SURFACE DRAG AND SWARMING BACTERIA

A Dissertation

by

KATIE MARIE FORD

Submitted to the Office of Graduate and Professional Studies of
Texas A&M University
in partial fulfillment of the requirements for the degree of

DOCTOR OF PHILOSOPHY

Chair of Committee,	Pushkar P. Lele
Committee Members,	Arul Jayaraman
	Michael D. Manson
	Beiyan Nan
Head of Department,	Arul Jayaraman

May 2021

Major Subject: Chemical Engineering

ABSTRACT

Escherichia coli swarm on semi-solid agar surfaces with the aid of flagella. One hypothesis suggests swarmer cells may overcome the increased viscous drag near surfaces by developing higher flagellar thrust and by promoting surface wetness with the aid of a flagellar switch. The switch enables reversals between clockwise (CW) and counterclockwise (CCW) directions of rotation of the flagellar motor. Here, we measured the behavior of flagellar motors in swarmer cells in response to semi-solid surfaces. Results indicated that although the torque was similar to that in planktonic cells, the tendency to rotate CCW was higher in swarmer cells. This suggested that swarmers likely have a smaller pool of phosphorylated CheY. Results further indicated that the upregulation of the flagellin gene was not critical for flagellar thrust or swarming. Consistent with earlier reports, moisture added to the swarm surface restored swarming in a CCW-only mutant, but not in a FliG mutant that rotated motors CW-only ($FliG^{CW}$). Fluorescence assays revealed that $FliG^{CW}$ cells grown on agar surfaces carried fewer flagella than planktonic $FliG^{CW}$ cells. The surface-dependent reduction in flagella correlated with a reduction in the number of putative flagellar preassemblies. These results hint toward a possibility that the conformational dynamics of switch proteins play a role in the proper assembly of flagellar complexes and flagellar export, thereby aiding bacterial swarming.

Next, we utilized blinking optical tweezers and colloidal probes to indirectly measure the viscous drag associated with the semi-solid agar surfaces which *Escherichia*

coli swarm on. *E. coli* are known to swarm over a very fine range of agar concentrations. One hypothesis proposes that this sensitivity to agar concentration is associated with an increasing viscous drag as agar concentration increases. Moreover, there are numerous studies that suggest increased viscous load may play a role in the induction of swarming. We found that semi-solid agar surfaces behave remarkably similarly to no-slip glass surfaces; hence, the viscous drag experienced by swarming cells is likely very high. Finally, our findings suggest that viscous drag does not increase with agar concentration and is not responsible for *E. coli's* inability to swarm at higher agar concentrations.

DEDICATION

To my mom, dad, and sister for believing in me when I did not have the courage to believe in myself .

ACKNOWLEDGEMENTS

I would like to thank my committee chair, Dr. Lele, and my committee members, Dr. Jayaraman, Dr. Manson, and Dr. Nan for their guidance and support throughout the course of this research.

I would also like to thank all of my friends for their support and for putting up with me all of these years. Cody, Lani, Devon, Josh, Alex, Jamie, Andre, and Pablo – thank you for keeping me laughing. Thank you to my research group, special thanks to Jyot who read every book I ever suggested to him and then discussed them with me endlessly. Joshua, thank you for being you and cheering me on from near and far.

Finally, thanks to my family - Mom, Dad, Lyndsey, Corey – thank you for your encouragement, support, and endless love. This would not have been possible without you.

CONTRIBUTORS AND FUNDING SOURCES

Contributors

This work was supervised by a dissertation committee consisting of Dr. Pushkar Lele (advisor) and Dr. Arul Jayaraman of the Department of Chemical Engineering and Dr. Mike Manson and Dr. Beiyan Nan of the Department of Biology.

Chapter II is a part of the journal article "Switching and Torque Generation in Swarming *E. coli*". Jyot D. Antani, Aravindh Nagarajan, and Madeline M. Johnson helped with experiments and analysis.

Chapter III is a part of the manuscript "Surface Induced Drag on Motile Bacteria", currently in preparation. Ravi Chawla conducted initial experiments that laid the groundwork for this project and advised on experimental design. Kelly Mowery assisted with data clean-up and analysis.

Appendix E is the journal article "Biophysical Characterization of Flagellar Motor Functions". Ravi Chawla assisted in experiments and preparation of the article.

Kelly Mowery helped proof-read and format this document. She also helped check references and aided in checking the document for consistency and accuracy.

All other work conducted for the dissertation was completed by me under the supervision of Dr. Pushkar Lele.

Funding Sources

This work was supported in part by grants from Texas A&M Engineering Experiment Station (TEES) start-up funds, the National Institute of General Medical Sciences of the National Institutes of Health under award number R01GM123085, and

from NSF-GRP, DGE 1252521. The funding agency had no role in study design, data collection or interpretation, or the decision to submit the work for publication. Any opinion, findings, and conclusions or recommendations expressed in this material are those of the author and do not necessarily reflect the views of the National Science Foundation and the National Institute of Health.

NOMENCLATURE

Amp	Ampicillin
BLAST	Basic Local Alignment Search Tool
CCD	Charge-coupled device
CCW	Counterclockwise
CW	Clockwise
CWbias	Clockwise bias
DLS	Dynamic light scattering
Kan	Kanamycin
LB	Lysogeny broth/ Luria Bertani media
LPS	Lipopolysaccharides
MB	Motility Buffer
MSD	Mean-squared-displacement
PCR	Polymerase chain reaction
PMT	Photomultiplier
PYE	Peptone yeast extract
TB	Tryptone Broth
TIRF	Total internal reflection fluorescence
YFP	Yellow fluorescent protein

TABLE OF CONTENTS

Page

LIST OF FIGURES

Page

LIST OF TABLES

Page

1. INTRODUCTION

Motile bacterial species are often thought about and studied in terms of their planktonic, liquid grown, states; however, these species often spend the majority of their lives in close proximity to surfaces [1]. In response to these surfaces, many species adapt their behavior and are capable of undergoing significant changes that give rise to surface motility. Bacterial surface motility and the ability to colonize surfaces provide distinct ecological advantages to bacteria: biofilm formation can protect bacteria from environmental stresses, antibacterial agents, and antibiotics [2, 3], gliding aids in regulating growth under starvation conditions [4], and swarming gives rise to elevated resistance to a wide variety of antibiotics [5-7]. In some cases, the advantages of surface motility confer the ability to colonize the human body. One noteworthy example is the implication of swarming in infections of the urinary tract [8].

Liquid grown bacteria predominately rely on flagella-driven 3D motility in bulk fluids, but when they are introduced to soft agar surfaces, some bacterial species swarm. Swarming is a surface-dependent 2D group motility marked by morphological changes and cell rafting. Swarming is studied on agar surfaces in the laboratory and the range of concentrations of agar over which bacteria can swarm allow swarmers to be divided into two groups – "robust" and "temperate" swarmers [9]. Robust swarmers can swarm on agar concentrations as high as 2% [10] while temperate swarmers require softer surfaces [8]. *Escherichia coli*, an example of a temperate swarmer, swarm over a very fine range of

Eiken agar concentrations (0.45-0.5% w/v agar) but are unable to swarm at higher concentrations of agar and on other types of agar [11].

The inability of *E. coli* to swarm at greater agar concentrations may be related to their ability, or lack thereof, to overcome increased viscous resistance at higher agar concentrations [12]. Other species of temperate swarmers produce surfactants to overcome hydrodynamic forces between the cell and the agar [13]. *E. coli* are not known to produce surfactants when swarming, making surface wetness a crucial factor. One widely accepted theory concerning surface wetness is that the chemotaxis machinery, which enables switches in the direction of rotation of the flagellar motor in response to external stimuli, aids the cells in drawing moisture from the agar and surrounding cells [14, 15]. There is sufficient evidence to support the notion that mutants with motors which rotate in only one direction cannot swarm under normal assay conditions but swarming can be rescued through the addition of moisture to the surface [16, 17]. Moreover, switching aids in reversals which are essential for swarming [18]. Yet, it has recently been shown that swarming cells can reverse directions without motor switching [19]. Despite the many theories surrounding the role that switching plays in swarming, the true function of switching in aiding swarming remains unclear. In Chapter 2, we characterize the motors of swarming cells and show that they rotate almost exclusively in a single direction.

When swarmer cells are removed from agar substrates and returned to liquid cultures they revert to their planktonic states [20]. Therefore, proximity to substrates is a likely trigger for the transition between planktonic and swarmer cells. Surface sensing, or the ability of a cell to “feel” that it is on or near a surface, is likely a cue for swarming in

other bacterial species. In some species of bacteria, increased viscous drag due to surfaces is thought to prompt intracellular signaling that results in swarmer cell differentiation [9, 20-22] . The importance of agar concentrations and surfactants in swarming support the notion that sensing of external stimuli, such as the increased viscous drag associated with surfaces, are imperative for swarming and, indeed, this seems to be the case [12].

While agar surfaces are believed to represent a high load condition on the flagellum [23, 24] this theory is untested. Surface drag has been measured for simple geometries near no-slip surfaces, such as single latex beads near a solid glass boundary [25]. The glass surface represents a no-slip condition, where the fluid layer immediately adjacent to the glass boundary is stationary and does not allow flux through the surface. Such measurements seem unlikely to be representative of agar surfaces as agar is soft and porous [26]. Thus, the current understanding of viscous drag near agar surfaces is lacking. As mentioned previously, *E. coli* only swarm over a narrow range of concentrations of Eiken agar (0.45-0.5 % w/v). Intuitively, one does not expect to observe drastic changes in viscous drag when going from 0.45% w/v agar to 0.55% w/v agar. In Chapter 3, we measured surface drag with a single latex bead near agar surfaces and demonstrated there are no significant changes in viscous drag between 0.45% w/v agar surfaces and 1% w/v agar surfaces. Additionally, we show that agar surfaces behave similarly to no-slip surfaces. We use a novel technique which orients the agar surface perpendicular to the focal plane and allows for spatial awareness in the z plane.

Other than swarming, biofilm formation is also triggered by surface sensing [27]. As previously stated, biofilm formation can protect bacteria from a variety of

environmental stresses [2, 3]. Biofilms are communities of bacteria that are irreversibly attached to a surface and can become 10-1000 times more resistant to antimicrobial agents [28, 29]. They often form on medically implanted devices such as catheters and joint prostheses [30, 31] and can be lethal, making them a major medical concern. Similar to swarming, proximity to surfaces is likely a key factor in the initiation of biofilm formation [27]; however, biofilm formation can also begin in response to other environmental signals [32].

Caulobacter crescentus, a fresh water bacterial species, is among the best-studied examples for surface sensing-induced biofilm formation. *C. crescentus* swim by rotating a single polar flagellum, which is believed to be involved in detecting increased viscous drag near surfaces. Once the cell detects the change in the viscous drag, it sheds the flagellum, generates a stalk and secretes an adhesive polysaccharide holdfast necessary to irreversibly attach to the surface [33, 34]. However, at present, it is not possible to probe the response of the flagella to surface attachment in *C. crescentus.* We are interested in overcoming the status quo and developing a sticky variant of a flagellin protein in *C. crescentus*, which we envision will enable us to experiment on single flagellar motors. In Chapter 4, we describe our preliminary efforts to genetically design a sticky flagellum in this species.

2. SWITCHING AND TORQUE GENERATION IN SWARMING *E. COLI*

2.1 Introduction

Swarming in flagellated bacteria is a type of surface-dependent motility that is marked by rapid and coordinated movements of groups of cells in coherent structures and swirling patterns on top of semi-solid surfaces [35]. Swarming has been implicated in several types of infections [36-38], as well as elevated antibiotic resistance [5, 7, 39, 40]. The initiation of swarming is preceded by the arrival of planktonic cells on a surface – in a laboratory setting this involves the inoculation of planktonic cells on agar substrates [41]. Subsequently, the planktonic cells transition into a swarmer state [42]. The swarmer state is often accompanied by, depending on the bacterial species, elongation of the cell body, expression of more number of flagella, multi-nucleation, and secretion of polysaccharides that promote surface motility [8, 43, 44]. In *E. coli,* swarmer cells reportedly double their lengths but maintain similar flagellar numbers per unit surface area as the planktonic cells. Due to the proximity of the swarmer cells to a solid surface, the viscous drag experienced is likely high [23, 24]. It is unclear how cells overcome surface drag but one possibility is that motors in swarming bacteria adapt to produce higher torque than motors in planktonic cells [45], although this remains untested. Another way that cells might overcome the drag is with the aid of the flagellar switch – it is known that the ability of the motor to switch its direction of rotation between clockwise (CW) and counterclockwise (CCW) is vital for swarming. Mutants that rotate motors CCW-only or CW-only fail to swarm whereas those that are able to switch their motors are able to swarm [16, 46]. It has been proposed that switching aids in the lubrication of the surface by

extracting water from the underlying agar, and possibly helps liberate cells from the secreted LPS (lipopolysaccharides), thereby facilitating cell movement [15, 47]. Much of this remains unexplained and these are unlikely to be the only mechanisms of drag reduction employed by swarming bacteria [48].

The flagellar motor rotates with the aid of stator units. Experiments in planktonic cells have shown that motors recruit stator units in greater numbers when the viscous loads are higher [49-51]. Mechano-sensitive stator recruitment is one way to adapt torque in response to increased viscous drag near surfaces [52]. However, motor-torque in swarming bacteria has never been measured. Torque enables the rotation of extracellular filaments, resulting in a thrust on the cell body. Proper motor and filament assembly is, therefore, the key in coupling torque and cell-propulsion. The initial steps in motor-assembly include the formation of the FliG, FliM and FliN complexes that form the flagellar switch [53-56]. Concurrently, parts of the flagellar export apparatus begin to form with the final components, FliI, FliH and FliJ, assembling prior to the formation of the flagellar hook [57, 58]. The export complexes associate with FliN through the export apparatus component, FliH [59-61]. Following the assembly of the rod and the flagellar hook, with a remarkable precision [62, 63], the anti-sigma factor FlgM is exported. This activates FliA, resulting in the transcription of class 3 genes including the flagellin protein, FliC, which forms the extracellular filament [64, 65].

Reversals in the direction of rotation of the extracellular filament are mediated by the binding of an intracellular response regulator, CheY-P, to FliM and FliN, which promotes CW rotation in an otherwise CCW-rotary motor [66, 67]. Biasing of the flagellar

rotation in either the CCW or CW direction is known to cause remodeling of the flagellar switch-complex, independent of CheY-P binding [68]. The number of FliM and FliN subunits is fewer in motors that are locked in the CW direction and higher in the motors that are locked in the CCW direction [68-72]. Estimates indicate that there are numerous putative flagellar preassemblies in a planktonic cell [73, 74], although only 3-4 exhibit complete flagellar assembly. It is unclear if there is a role for the remodeling of FliM and FliN in swarming, however, deficiencies in the flagellar switch-assembly do hamper filament formation [75].

Here, we characterized torque generation and flagellar switching in swarmer cells of *E. coli.* Our measurements with wildtype *E. coli* indicated that the magnitude of torque generated in swarmer cells was similar to that in planktonic cells. However, the CW_{bias} (fraction of time that the motors rotate CW) was much lower in swarmer cells compared to that in planktonic cells. This reduction was dramatic, with ~ 30% of the swarmer cells rotating CCW-only. Despite the preference for CCW rotation in the swarmer-state, the wildtype strain swarmed on agar substrates, whereas a CCW-only strain was unable. In agreement with earlier reports [14], the CCW-only strain could swarm in the presence of additional moisture on the agar surface. Experiments further indicated that transcriptional upregulation of the flagellin gene was neither critical for developing adequate flagellar thrust in the swarmer state nor for swarming. However, a CW-only mutant that rotates its motors exclusively CW due to a mutation in *fliG* [76] could not swarm irrespective of the surface conditions. Using fluorescence visualization techniques, we found that the $FliG^{CW}$ planktonic cells expressed fewer filaments compared to their wildtype planktonic

counterparts. The number of FliG^{CW} filaments was even lower when the strain was grown on agar surfaces, which correlated with a reduction in the number of putative preassembled flagellar complexes. It is possible that flagellar assemblies in agar-grown cells are influenced, at least partially, by the conformations of the monomeric FliG subunits.

2.2 Materials and Methods

2.2.1 Bacterial Strains and Plasmids

Bacterial strains were derived from either RP437 or AW405 parent *Escherichia coli* strains (Table 2-1). All plasmids were prepared with the pTrc99A vector backbone. Chromosomal alterations were achieved with the λ-red mediated homologous recombination technique [77].

Table 2-1: Bacterial strains.

Strain/Plasmid°	Background	Genotype	Source
CCW strain⸸	RP437	Δ*cheY*	This work
CW strain⸸	RP437	Δ*cheRcheBcheZ*	This work
FliG^{CW} strain⸸	RP437	*fliG^{CW}*	Howard Berg lab
HCB1737	AW405	*fliC^{Cys}*	Howard Berg lab
VSJ207 (FliG^{CW})*	AW405	Δ*cheY*, *fliG^{CW}*, *fliC^{Cys}*	Howard Berg lab
FliG^{CW} *fliM-Y-fliM*	RP437	fliG^{CW},*fliM-eYFP(A206K)-*	This work
fliM-Y-fliM, *CheY***	RP437	*fliM-eYFP(A206K)-fliM,* CheYD13KY106W	This work
HCB909	pXYZ202	CheYD13KY106W	Howard Berg Lab
pPL1	pTrc99A	*fliG^{CW}*	(Lele & Berg, 2015)
pPL14	pTrc99A	*motAmotB*	(Lele & Berg, 2015)

pPL33	pTrc99A	*fliA*	This work
pPL40	pTrc99A	*fliF*	This work
pPL42	pTrc99A	*fliI*	This work
pPL47	pTrc99A	*flhA*	This work

ǂ Corresponding strains were prepared to carry the $fliC^{sticky}$ allele to enable flagellar tethering and motor assays.

* A cysteine replacement in the native *fliC* allele enabled fluorescent labeling of the flagella

° All plasmids were pTrc99A-based.

2.2.2 Media

Overnight cultures were grown from isolated colonies in 5 mL of Tryptone Broth (TB) at 30 °C. Day cultures were grown by diluting 100 µL of overnight culture in 10 mL of fresh TB at 33 °C to OD_{600}~0.5. Swarm-agar plates (Peptone, 10 g/L; NaCl, 5 g/L; Beef extract, 3 g/L; 0.45% Eiken Agar, 0.5% Glucose) were prepared fresh, poured, and allowed to dry for 20 minutes open-faced on the work bench prior to inoculation with the strain of interest (2 µl, overnight culture grown at 30 °C). Motility buffer (0.01 M Phosphate buffer, 0.067 M NaCl, 10^{-4} M EDTA, 0.01 M Sodium Lactate and 1 µM Methionine, pH~7.0) was employed in motility assays.

2.2.3 Motility Assays

Tethered motors: Cells were prepared for tethered cell-assays by washing several times in motility buffer followed by shearing of the flagella, as described previously [78]. Flagellar tethering to beads or coverslips was achieved with a sticky *fliC* mutation [79]. Cell-rotation was imaged and recorded on a Nikon Eclipse Ti-E with a 20x phase objective or a Nikon Optiphot with a 40x phase objective at ~60 fps with a CCD camera (DCC1545M-GL, Thorlabs Inc). Bead-rotation was imaged on a Nikon Optiphot with a 60X phase objective coupled to a photomultiplier setup [78, 80].

Swarming: Swarm-assays were carried out in an environmental chamber (ETS Model 5472, Electro-Tech Systems, Inc) that allowed for a precise control over humidity and temperature. Swarm-plates were incubated for 8-10 hours following inoculation at 75% relative humidity and 30 °C, and then allowed to dry open faced for 2-4 hours to increase the density of growth before imaging with a gel imager (ChemiDoc Touch Imaging System, BioRad). To add moisture to the agar surface, plates were sprayed with water from a spray bottle until the agar-surface was visibly wet. The surface was allowed to dry with the lid open for one minute before inoculation. The amount of water added in such an approach was 0.38 ± 0.03 mL. As an additional check, swarming was visually confirmed by observing colony movement within a region of the swarm plate with a 40x phase objective on a Nikon Optiphot Microscope.

Swimming: Planktonic cells were diluted in either fresh TB (1:10 dilution) or suspended in motility buffer. The dilute suspension was observed in a standard flowcell and cell-motion was recorded away from either surface (coverslip or the microscope slide) at ~60 fps with a CCD camera (DCC1545M-GL, Thorlabs Inc). In the case of swarmer

cells, cells were recovered from swarm plates by gently pouring 10 mL of motility buffer on the agar surface and swirling to dislodge surface-associated cells. Experiments were also done where cells were recovered specifically from the leading edge of the swarm and from the center of the colony; however, the CW_{bias} was similar in cells recovered from the two areas. The supernatant was collected in a Falcon tube and introduced in a flow cell for observation under a Nikon Optiphot microscope.

2.2.4 Fluorescence Microscopy

A Nikon Ti-E microscope with a 100 mW, 514 nm laser (Cobalt Fandango) focused in the back focal plane of a 60x TIRF objective was used to generate evanescent fields. An Andor iXon DU897 camera was used for capturing TIRF (total internal reflection fluorescence) images while a CCD camera (DCC1545M-GL, Thorlabs Inc.) was used for capturing phase contrast images. Strains carrying *fliC*^{cys} were labeled with maleimide dye as described elsewhere [81]. The *fliM-eYFP-fliM* internal fusion was gifted to us by the Berg lab. The allele carried a [Gly Gly Gly][YFP_{Ser}…YFP_{Lys}][Ser Gly Gly Gly] insertion between codons 15 and 16 of *fliM*. Tethered motor assays indicated that the fusion motors were fluorescent and functional.

2.2.5 Motor stall assays

Optical traps were generated with a 976 nm laser (Azurlight ALS-IR-976-10-I-SF) by overfilling the back-aperture of a 60x objective. Optically-trapped beads or cell bodies were then used to physically interrupt the rotation of tethered cells by moving the trapped object in the path of a rotating cell. The trap strength was adequate to prevent rotation of all tethered cells. When the traps were turned off, the cell body was free to rotate again.

2.2.6 Isolation of RNA and preparation of cDNA

Prior to extraction, bacterial strains were grown in fresh liquid swarm medium at 30°C or grown on solid swarm plates as previously described. All swarm assays for directionally-biased cells were carried out by adding moisture and cells were only collected from plates that indicated successful swarming. Cell suspensions were centrifuged at 1000 g for 3 minutes, re-suspended in RNAlater® and stored at 4°C for 1 day, after which time cells were transferred to -80°C for storage. RNA was extracted using an illustra RNAspin Mini Kit manufactured by GE Life Sciences. RNA was quantified using a NanoDrop 2000c (ThermoFisher Scientific) and a sample was run on a gel to check for ribosomal bands. The RNA was then converted into cDNA using qScript cDNA SuperMix manufactured by Quantabio. Separate reactions were carried out for the gene of interest –*fliC* (5'GCACCACCAGCATCGTTTGTAGTT3') and the housekeeping gene –*gapA* (5' ACCGGTAGAAGACGGGATGATGTT3').

2.2.7 Real-time PCR

A LightCycler® 96 Real-Time PCR System (Roche) was employed for real-time PCR. Each reaction (20 µl) was carried out in a 96-well optical grade PCR plate, sealed with optical sealing tape. Amplifications were carried out using SYBR® Green JumpStart™ Taq ReadyMix™ manufactured by Sigma-Aldrich, 2 µl of cDNA and 250 nM of each primer (see primer information in Appendix A, Table A-1). Three biological and two technical replicates were carried out for each strain in planktonic and swarming cells. Relative quantification was performed by the $\Delta\Delta C_T$ method.

2.2.8 Data Analysis

Videos of tethered cells were analyzed with custom-written codes in MATLAB to find the rotational speed as a function of time [82]. Time-averaged CW_{bias} values were determined for each tethered motor over the duration of 1-2 minutes. Mean speeds for cells were determined from Gaussian fits to speed-distributions. *Swimming*: Most cells swam in straight lines for limited time-periods in the liquid medium. For each cell, the frames over which straight-line motion was observed were averaged which resulted in a single image with bright streaks on a gray background. The corresponding length of the straight-line intensity profile was determined and divided by the period of observation to obtain swimming speed.

2.2.9 Statistical analysis

All statistical analyses were performed with the Student's T-test. Results with $p < 0.05$ were considered statistically significant.

2.3 Results

2.3.1 Flagellar switching in swarmer cells

Previous research indicated that the flagellar switch is able to adapt to mechanical stimuli, although the mechanisms are presently unknown [49, 83]. To determine how cells adapt flagellar motor functions in order to continue their surface existence, we characterized motor behavior in swarmer cells. We inoculated overnight cultures of a wildtype strain (RP437 background) that carried a sticky *fliC* allele on standard swarm agar plates. The colonies swarmed and were recovered from the plates several hours later, as discussed in the Materials and Methods section. The swarmer cells were then sheared and washed in motility buffer, before tethering to glass surfaces. The CW_{Bias} (fraction of

time that motors rotate CW) was quantitatively determined from digital recordings of cell rotation with custom-written MATLAB codes [72]. Reversal frequencies were also determined. As shown in Figure 2-1A, the average CW_{bias} in swarmer cells (left panel) was lower than that in the corresponding planktonic cells (right panel). The distribution in the case of the former was skewed towards a $CW_{bias} \sim 0$, with 36% of cells rotating CCW-only. The reversal rates further illustrated this disparity. Figure 2-1B indicates that the reversal rates were lower in case of the swarmer cells (left panel) compared to those observed in the planktonic cells (right panel). These observations are consistent with a recent work that observed lower tumbling frequencies in swarmer cells in comparison to planktonic cells grown in a liquid medium [84]. This result is unexpected considering that switching of the flagella has been reported to be crucial for swarming [16]. The lower CW_{bias} likely indicates that the pool of phosphorylated CheY may be reduced in swarmer cells in comparison to planktonic cells, although differential acetylation levels could also play a role [85].

To test the role of the flagellar switch in swarming, several directionally-biased mutant strains were constructed from the parent AW405 and RP437 wildtype strains. In general, two types of strains were employed in swarm-experiments: a strain lacking *cheY* in which motors rotated exclusively CCW (***CCW strain***) and a *fliG* mutant strain in which motors rotated exclusively CW (***FliG^{CW} strain***) because the FliG subunits were locked in the CW conformation [72, 76]. In addition, a strain lacking *cheR-cheB-cheZ* was also constructed in which motors rotated predominantly CW (***CW strain***) due to an excess of [CheY-P] [86]. As anticipated, all the directionally-biased mutants failed to swarm in a

standard swarm assay, unlike the wildtype strains. Swarming was restored in the CCW strain when CheY was expressed from an inducible plasmid. In agreement with earlier reports [14], it was possible to restore swarming, at least partially, in the CCW and CW strains by moistening the agar surface with water (see Materials and Methods and Figure A-1, Appendix A). Next, the CCW strain was transformed with an inducible vector from which a constitutively-active form of CheY (CheYD13KY106W) was expressed [79]. Background expression was adequate to predispose tethered cells in this strain to rotate CW-only. It was possible to restore swarming partially in this strain by adding moisture. Conversely, swarming could not be restored in the $FliG^{CW}$ strain. These results suggested that the ability to swarm was not completely inhibited by switch-inactivation in strains that carried the wildtype *fliG* allele. However, the CW conformation of the monomeric FliG subunits in the $FliG^{CW}$ strain probably precluded swarming.

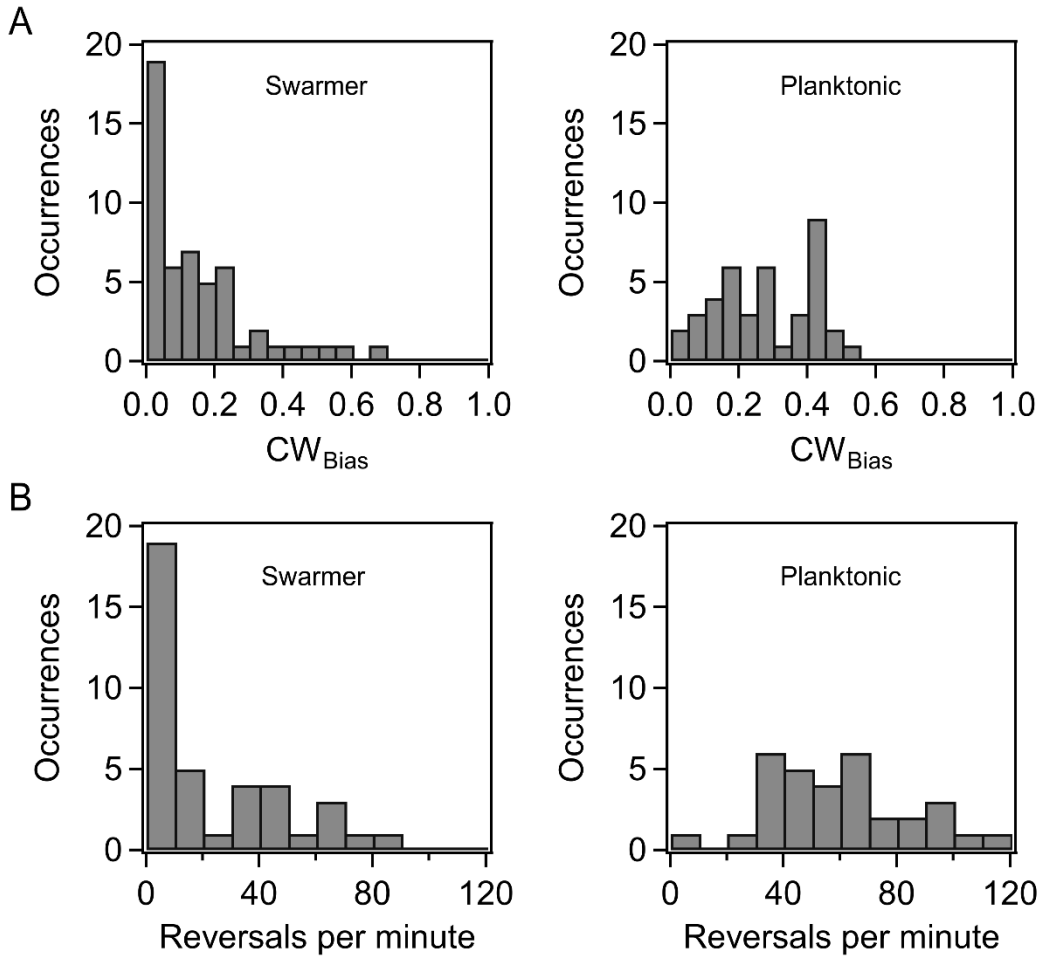

Figure 2-1: Probability of CW rotation and reversal rates for WT swarmers. A) Probability of CW rotation in wildtype swarmers and planktonic cells. The mean CW_{Bias} was 0.27 ± 0.02 (n = 40 motors) for the wildtype planktonic cells and 0.15 ± 0.02 (n = 52 motors) for the wildtype swarmer cells. The difference in the mean CW_{Bias} for planktonic and swarmer cells was significant ($p < 0.05$) B) Distribution of motor reversals observed in wildtype swarmer and planktonic cells. The mean reversal rates were 22.4 and 59.9 reversals/min, respectively. The difference in the means was significant ($p < 0.05$).

2.3.2 Torque and swarming

In order to determine if the loss in swarming ability in the directionally-biased mutants was, in part, due to an emergent deficiency in torque generation following surface-inoculation, we measured the speed of rotation in tethered cells that had been

recovered from agar substrates. Based on the size of the cells and the mean speeds, we calculated the average torque generated in the CCW and CW strains (see Materials and Methods). As indicated in Figure 2-2A, there were no significant differences in the mean torques generated in the planktonic and the agar-grown cells, irrespective of whether they belonged to the CCW or CW strain. The same was true in the case of the wildtype planktonic and swarmer cells (data not shown). In the FliG^{CW} strain, we measured the mean torque over a range of viscous loads. The viscous load was varied by employing latex beads of different sizes (2, 1 and 0.75 μm) and rotation rates were measured via a photomultiplier-based high speed tracking technique [78, 80]. Torque was calculated from rotation speeds and bead sizes [87]. As shown in Figure 2-2B, the differences between the mean torque generated by the FliG^{CW} motors and that developed by the CW and CCW motors were statistically insignificant at high loads (load = 147.10 pN.nm.s). At lower loads (19.31 pN.nm.s), these differences were significant - FliG^{CW} motors produced ~15% less torque than the CW motors. At the lowest loads we employed (8.55 pN.nm.s), the difference between the average torque in FliG^{CW} motors and that in the CW strain was again insignificant, whereas that between the FliG^{CW} motors and the CCW strain was significant, as expected from the anisotropy in torque generation in the two directions of motor rotation [72, 80]. To assess if the complete inhibition of swarming in the FliG^{CW} strains arose due to such minor variations in torque, we transformed the FliG^{CW} strain with an inducible plasmid carrying the *motAmotB* genes. Higher expression of MotA-MotB levels increased the average torque in the FliG^{CW} strain to a level that was similar to that in the CCW strain (load = 19.31 pN.nm.s, Figure 2-2C). Yet, the same level of induction

failed to restore swarming in the FliG^{CW} strain. Together, the results indicated that swarmers are unlikely to develop higher flagellar power compared to planktonic cells at a given viscous load, in order to compensate for the increased surface drag.

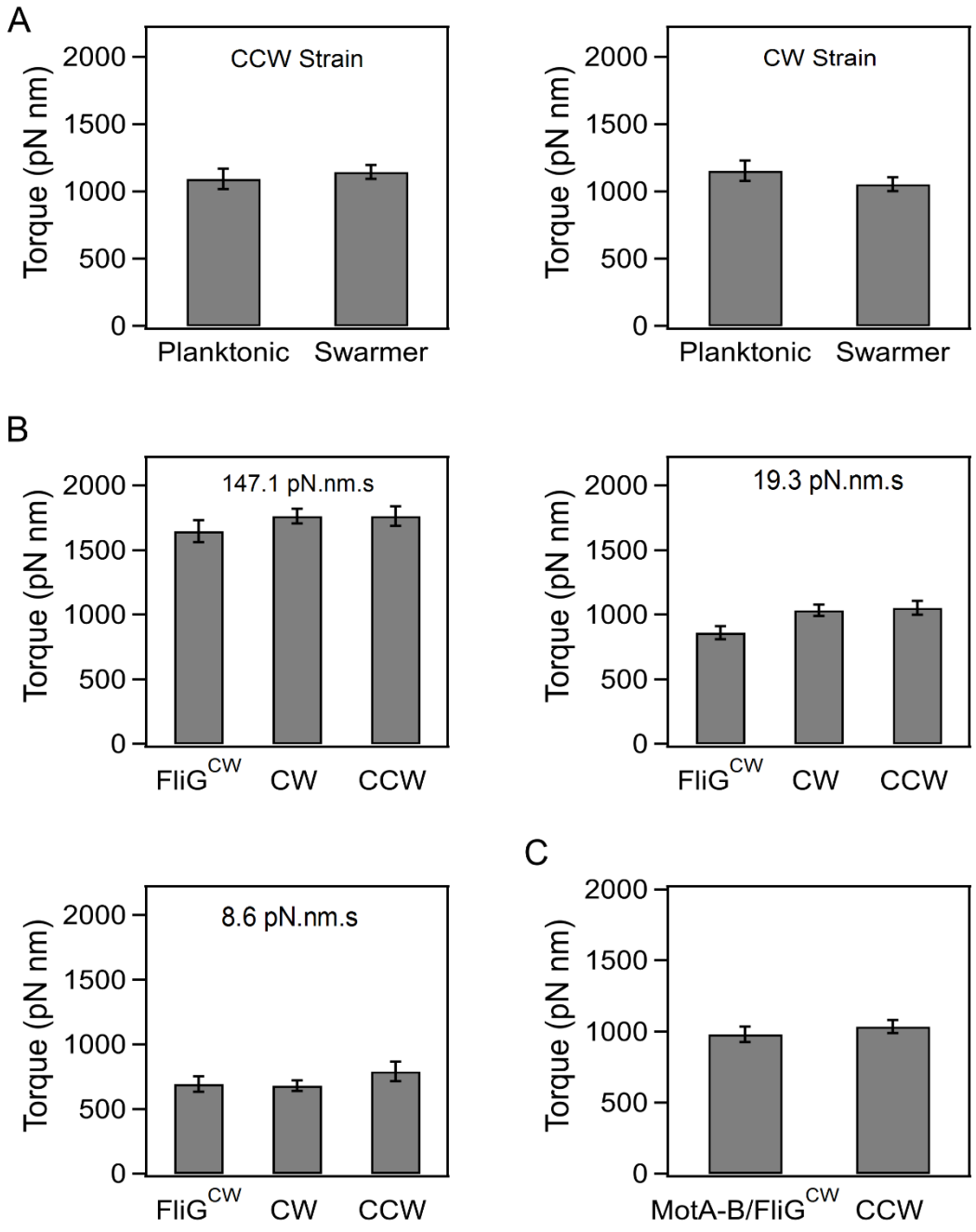

Figure 2-2 Average torque generated for cells at varying viscous loads. A) Average torque generated in planktonic and swarming cells belonging to the CCW and CW strains. The average torque was 1154.9 ± 75.4 pN nm (n = 35 motors, swarmer CCW strain) and 1121.7 ± 57.9 pN nm (n = 32 motors, planktonic CCW strain). Differences in the mean torques were not significant ($p > 0.05$). The average torque was 1093 ± 81.5 pN nm (n = 35 motors, swarmer CW strain) and 1144.5 ± 129.1 pN nm (n = 16 motors, planktonic CW strain). Differences in the mean torques were not significant ($p > 0.05$). B) Torque generated by the $FliG^{CW}$ strain in comparison to that in CCW and CW strains. At high loads (147.1 pN.nm.s), the differences in means were statistically insignificant. At medium loads (19.3 pN.nm.s), the differences in the mean torque in the $FliG^{CW}$ strain and the other strains were significant. At lower loads (8.6 pN.nm.s), the difference in the mean torque in the $FliG^{CW}$ strain and the CCW strain was significant. C) The slight degradation in the torque in the $FliG^{CW}$ strain seen in (B) was remedied by expressing extra copies of MotA and MotB subunits in the strain from an inducible plasmid. The difference in mean torques in this strain and the CCW strain was insignificant at a load of 19.3 pN.nm.s. All plots indicate standard error.

2.3.3 Flagellar thrust in agar-grown cells

Although our data suggests that differential torque generation is not the reason for the loss of swarming in directionally-biased mutants, a reduction in flagellar thrust could play a role. Flagellar thrust depends on a rich interplay between the polymorphic form, arc-lengths of the filament, filament numbers, and the ability to form tight flagellar bundles. Rather than making independent measurements of each of these factors, we opted to measure swimming speeds of the cells. The speeds encompass each of the key factors that influence motility, including cell lengths, enabling comparisons between different types of cells. To do this, swimming speeds were measured in the planktonic and agar-grown cultures in all the aforementioned strains. Agar-grown cells were recovered by adding and gently swirling motility buffer on the swarm substrates. Motility was subsequently recorded in standard flow cells and quantitatively analyzed; the data is shown in Table 2. Speeds measured in strains that were able to swarm on agar and were

able to swim in motility buffer have been labeled as *'swarmer speeds'*. Speeds measured in strains that did not swarm but were able to swim in motility buffer have been labeled as '*non-swarmer speeds'*. Speeds measured in strains that were grown in liquid media have been labeled '*planktonic speeds*'. There was no significant difference in the mean speeds measured in planktonic cells belonging to the directionally-biased strains carrying the native *fliG* allele and the wildtype cells. However, the difference in the mean speeds in planktonic cells belonging to the $FliG^{CW}$ and the wildtype strains was statistically-significant; $FliG^{CW}$ swam at ~33% lower speed. This indicated degradation in the flagellar thrust in $FliG^{CW}$ planktonic cells. In the case of cells recovered from the agar surfaces, the differences between the mean speeds in $FliG^{CW}$ and the wildtype were further amplified. The wildtype swarmer cells experienced an increased flagellar thrust by ~ 9% relative to the wildtype planktonic cells. In contrast, the agar-grown $FliG^{CW}$ cells were mostly non-motile. Amongst the ones that exhibited motility, the average swimming speed was ~1/2 the speed of the wildtype swarmers. In comparison, CCW and wildtype swarmer speeds were similar but the CCW non-swarmer speed was ~ 20% lower than the wildtype swarmer speed. This suggested that the inhibition of swarming in the CCW mutant (in the absence of added moisture) was partially-attributable to reduced flagellar thrust. Considering that the flagellar motor torque is not deficient, this indicated a degradation in either the flagellar lengths or the number of flagella in the directionally-biased mutant. In the case of $FliG^{CW}$, this deficiency was extreme. In the wildtype, there was no significant difference in the swimming speeds of swarmers in the presence or absence of added moisture on the agar surface.

Table 2-2: Mean swimming speeds for planktonic and agar-grown cells.

Strain name	Planktonic	Non-swarmer	Swarmer
Wildtype	24.5 ± 0.5 (n = 40)	-	26.7 ± 1.0 (n = 30)
CCW	22.4 ± 0.5 (n = 30)	21.7 ± 1.0 (n = 30)	26.4 ± 0.8 (n = 30)
fliG^{CW}	16.5 ± 0.6 (n = 30)	15.3 ± 0.6 (n = 30)	-

2.3.4 Loss of Swarming in FliG^{CW} mutant

2.3.4 1 Filament numbers

To determine why the flagellar thrust in the FliG^{CW} strain was dramatically lower in comparison to other strains, we employed fluorescence visualization techniques and measured the number of filaments in planktonic as well as agar-grown cells. Filaments carrying cysteine residues were labeled with a maleimide-based fluorescent dye and visualized as detailed in the Materials and Methods. The filament numbers were manually counted from the fluorescence microscopy images. The average number of filaments per cell in the planktonic FliG^{CW} strain was determined to be 3± 1 (Figure 2-3A). The average number in the planktonic wildtype cells was 4 ± 1 (not shown). Thus, there was ~ 25% drop in the number of flagella per cell in the planktonic FliG^{CW} cells. This was consistent with a 33% decrease in swimming speeds in the planktonic FliG^{CW} cells. In comparison, the distribution of the number of filaments per cell in the agar-grown FliG^{CW} strain was skewed towards zero (Figure 2-3A). Of the 200 cells analyzed, 115 cells (57.5%) appeared to carry no filaments. In the cells that had visible flagella, the average number of filaments per cell was 1.6 ± 0.1. In wildtype swarmer cells, only 12 cells out of 115 appeared to carry no filaments. In the cells that had visible flagella, the average number of filaments

per cell was 3.0 ± 0.2 (see Figure A-2,Appendix A), in agreement with recent measurements of wildtype *E. coli* swarmers by Turner and co-workers [84]. The reduction in the number of visible filaments in the FliG^{CW} cells was correlated with the complete loss of swarming ability. Additionally, upon visual inspection of these filaments, filaments appeared to be shorter than those found in wildtype cells.

2.3.4.2 Flagellar susceptibility to shear

One explanation for the lower filament numbers in the FliG^{CW} strain, planktonic or otherwise, could be that the flagellum is more susceptible to shear, similar to the reported propensity of the flagella to shear in *fliL* mutants of *Salmonella enterica* [88]. To test this hypothesis, we employed optical traps to stall tethered motors of the FliG^{CW} strain. Stalling ensures that the flagellar motor delivers the maximum possible force on the rotor [87], thereby subjecting the flagellum to high physiologically-relevant shearing forces. Several tethered motors were stalled for approximately 10 minutes (n = 10 cells), as described in the Materials and Methods. Shearing of the flagellum was expected to be detectable through the detachment of the cell from the surface during stalling or through the loss of the ability to rotate following the removal of the optically-trapped bodies. In all of the experiments, flagellar motors in the FliG^{CW} strain remained tethered and functional even after trap removal. This indicated that the FliG mutation is unlikely to result in flagella that are easily sheared under high viscous loads.

2.3.4.3 Intracellular protein levels

We tested whether incomplete or inefficient assembly of the export apparatus could be compensated for by increasing the expression levels of the export ATPase, FliI,

or the levels of FlhA. The latter is a part of the export gate of the type 3 secretion system and forms a dock for FliI [89]. FliI overexpression especially has been shown to partially restore flagellation in strains carrying partial deletions in the switch proteins [75, 90]. However, overexpression of these two proteins from inducible plasmids failed to restore swarming in the $FliG^{CW}$ strain (Figure A-3A and A-3B, respectively). Similarly, overexpression of FliF and $FliG^{CW}$ also failed to elicit swarming in that strain.

2.3.5 Flagellin regulation

The reduced flagellar thrust and filament numbers could arise due to a reduction in the flagellin levels in the directionally-biased mutants. To test this, qPCR experiments were performed as detailed in the Materials and Methods. Briefly, the flagellin gene was selected based on earlier reports that *fliC* was one of the only genes that is differentially regulated in wildtype swarmers in *Salmonella typhimurium* [91]. Comparisons were made between the transcriptional levels of *fliC* in the planktonic and swarmer cell types for each of the three strains: the wildtype, the CCW and the $FliG^{CW}$ strain. In the case of the CCW and the $FliG^{CW}$ strain, the cells were recovered from agar substrates that had been treated with water to increase moisture. Swarming was observed in the former but not in the latter strain. FliC mRNA levels were upregulated by twofold in wildtype swarmers, but there was no significant change in the two directionally-biased strains (Appendix A, Table A-2). It was interesting to note that although the flagellin gene was not significantly upregulated in the agar-grown CCW cells, unlike the wildtype, swarming was not inhibited. Flagellar thrust was not diminished in CCW swarmers either. We did not observe a downregulation in flagellin-transcription in the agar-grown $FliG^{CW}$ cells

(relative to the planktonic cells) despite a clear reduction in the number of filaments. These observations were further supported by swarm-experiments where *flgM* was deleted in the FliG^{CW} strain. The anti-sigma factor, FlgM, binds to FliA and prevents the transcription of class 3 genes. Inefficient functioning of the export apparatus could result in decreased FlgM export, preventing the transcription of flagellar genes. The Δ*flgM fliG^{CW}* strain however, failed to swarm; a wildtype strain deleted for *flgM* retained its swarming ability. Prior observations also suggest that the deletion of *flgM* in a CCW strain did not restore swarming [14]. Thus, a reduction in the expression of flagellar genes due to the inactivation of FliA by un-exported FlgM is unlikely to be the reason for the loss of swarming in the directionally-biased mutants. Instead, the data pointed to inefficient flagellar assembly as the key problem.

2.3.6 Flagellar preassemblies

2.3.6.1 FliM assembly in planktonic cells

Previous *in vivo* TIRF measurements with fluorescent fusions of FliM indicate that several putative flagellar preassemblies can be found throughout the cell membrane in planktonic cells of *E. coli*, although only 3-4 exist as complete flagella [73, 74]. These assemblies are identifiable as fluorescent foci [56]. In each functional motor, there are 34-45 molecules of FliM subunits [68, 74, 92, 93]. Remodeling of FliM is dependent on the direction of rotation of the motor and not on the interactions with CheY-P *per se* [68, 72]. The assembly of FliN is proportionate to that of FliM [70, 71]. The assembly of FliM is not disrupted in the FliG^{CW} mutant; previous observations indicate that the number of FliM subunits per motor in the FliG^{CW} strain is quantitatively similar to that observed in

wildtype motors that rotate CW-only due to an excess pool of phosphorylated CheY ([68] and Figure A-4). Furthermore, incomplete or deficient FliM assembly is known to degrade motor torque [94], whereas our torque measurements (Figure 2-2B and C) indicate little or no degradation in torque in FliG^{CW} motors, over the range of viscous loads studied here. It is likely, then, that the reduction in the number of filaments in planktonic cells of the FliG^{CW} strain, relative to the wildtype, is not due to a defective C-ring assembly. Rather, the reduction in filaments could be due to subtle changes in the interactions of the export apparatus with FliG-FliM-FliN protomers that have adopted a locked CW-conformation.

2.3.6.2 FliM assembly in cells grown on agar

Next, we attempted to determine whether the dramatic reduction in the number of filaments in FliG^{CW} cells grown on agar surfaces, relative to the planktonic FliG^{CW} cells, was entirely due to deficient flagellar export or whether the locked conformations of the FliG monomers inhibited the assembly of putative flagellar complexes on agar substrates. For this purpose, a FliG^{CW} strain was constructed that carried a genomic *fliM-eYFP-fliM* allele (Materials and Methods). Motors in this strain were functional and rotated CW-only when tethered. The strain was grown in liquid media and on agar surfaces. TIRF visualization enabled quantitative determination of the number of putative flagellar complexes with custom-written MATLAB codes for fluorescent foci detection [68]. The distribution of the number of foci detected per cell is indicated in Figure 2-3B for the planktonic and agar-grown FliG^{CW} cells. The average numbers of foci observed here are fewer than those reported earlier [74]. This is likely because the TIRF field employed only allows visualization of ~ 1/6th of the total volume of the cell body. As can be seen, there

were less than half the number of foci in the agar-grown cells (n = 28 cells) when compared with the planktonic cells (n = 29 cells). This is consistent with our observations of very few filaments in the agar-grown FliG^{CW} cells, and the loss of swarming in this strain. To further test this notion, we attempted to construct the corresponding wildtype control for fluorescence assays. However, that strain was unable to swarm and as a result, was not employed in further experimentation. Nonetheless, to test whether the FliG^{CW} mutation, rather than the CW-locked conformation of the FliG monomers, was responsible for the reduction in the foci on agar, we constructed and tested a strain that carried the native *fliG* and the *fliM-eYFP-fliM* alleles on its chromosome, and an excess of the constitutively-active CheY variant. Motors in this strain rotated CW-only and the strain did not swarm. A similar reduction in the number of foci in agar-grown cells was observed in comparison to the corresponding planktonic cells (Figure A-5). This suggested that it is not the FliG^{CW} mutation *per se* that interfered with the assembly of the putative flagellar assemblies in cells grown on agar surfaces, but possibly the lack of conformational transitions in the switch protomers. These experiments provide a measure of support to the notions that in cells that fail to swarm on agar, the number of putative flagellar preassemblies is decreased relative to that in the planktonic cells, and that the export of flagellar proteins is influenced by the conformations of the switch-protomers.

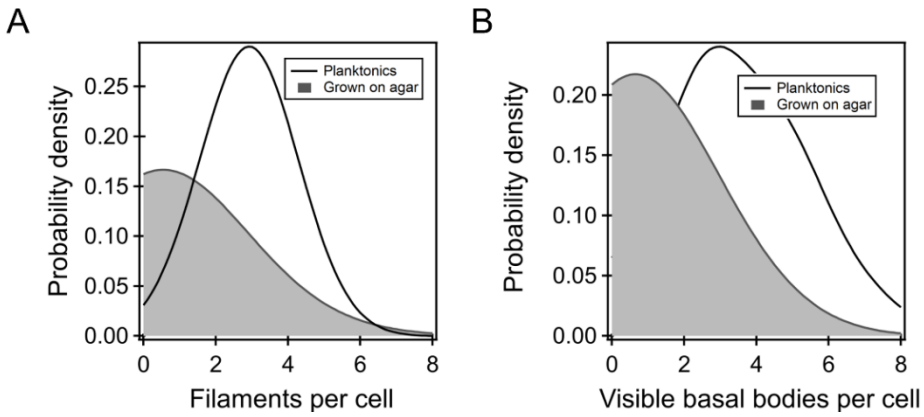

Figure 2-3: Filament and basal bodies per cell for FliG^{CW} cells. A) Kernel density estimates of the flagellar filaments per cell in the planktonic (black curve) and agar-grown FliG^{CW} strain (gray-shaded region). The difference in means was significant. Filaments were not observed in more than 57% of the agar-grown FliG^{CW} cells. The average filament number observed in the planktonic cells was lower than that observed in wildtype planktonic cells (4 ± 1). B) The number of putative flagellar preassemblies were determined from TIRF measurements. There were fewer such bodies in the agar-grown FliG^{CW} cells (number of preassemblies = 1.14 ± 0.2, n = 28 cells) relative to the planktonic FliG^{CW} cells (number of preassemblies = 2.48 ± 0.23, n = 29 cells), as seen from the kernel density estimates from the raw data. The difference in the means was significant ($p < 0.05$).

2.4 Discussion

Our results suggest that the flagellar motors in swarming cells of *E. coli* do not develop a higher power relative to the planktonic motors, for a given viscous load. This is in contrast to species such as *Pseudomonas Aeruginosa*, where cells employ a specialized set of stator proteins that are capable of developing higher power when the cell finds itself near a surface [95]. Unexpectedly, the CW_{bias} was lower in swarmer cells compared to that in planktonic cells, in fact, one out of three swarmer cells showed no inclination to reverse the direction of flagellar rotation. This is likely due to a smaller pool of phosphorylated CheY in the swarmer cells. This may be a consequence of an overall reduction in the

chemotaxis protein abundances, or a reduction in the sensitivity of the flagellar switch. In any scenario, the reduction in reversal rates and CW_{bias} is at odds with the swarm assays that clearly emphasize the role of flagellar switching in swarming. We propose, then, that it is not switching *per se*, but rather some associated property of the wildtype that enables swarming.

Our experiments also indicate that the transcriptional upregulation of the flagellin gene was neither critical for developing adequate flagellar thrust in the swarmer state, nor for swarming. This conclusion was derived from the observation that the CCW strain did not upregulate the expression of the flagellin gene, but was still able to swarm, provided that moisture was added. Swarmer cells belonging to the CCW strain were also able to generate similar flagellar thrusts as the wildtype swarmer cells. This suggested that the upregulation of *fliC* expression might simply be a consequence of agar-based growth of the wildtype strain. Transcriptional activity was also unchanged between the planktonic and swarmer cells belonging to the $FliG^{CW}$ strain. The deletion of *flgM* did not restore swarming in this strain. Considering that this strain was severely deficient in producing flagella on the agar substrate, this further suggested that the extreme defects in flagellar production on agar were unlikely due to reduced *fliC* expression. Optical tweezer experiments ruled out the possibility that the reduction in flagellar numbers in the $FliG^{CW}$ strain was due to shearing near the agar surface. The $fliG^{CW}$ mutation in planktonic cells of *E. coli* did not interfere with the assembly and functioning of the flagellar C-rings, as evidenced by previous measurements of FliM assembly in a $FliG^{CW}$ strain [68], and the torque measurements in the present work (Figure 2-2B and C). This suggested that the

locked CW-locked conformation of the FliG-FliM-FliN protomers, rather than assembly defects, affected flagellar export in this strain. Finally, we also found evidence that the assembly of putative FliM assemblies in the $FliG^{CW}$ cells was inhibited on agar surfaces, relative to the planktonic state. This decrease correlated with reduced flagellar numbers on agar surfaces, which was most likely responsible for the degradation in flagellar thrust and the loss of swarming. However, the corresponding wildtype fusion strain failed to swarm, which prevented us from determining if a high density of preassemblies was maintained in wildtype swarmers. Based on the available data, we speculate that flagellin export depends on the switch-activity, and not just assembly, and that the stochastic transitions in the conformations of switch protomers likely help anneal putative preassemblies. Under the conditions of increased shear near agar surfaces, locked protomeric conformations might result in inadequate assembly and inefficient export of flagellar substrates.

3. SURFACE INDUCED DRAG ON MOTILE BACTERIA

3.1 Introduction

In Chapter 1, we discussed the relationship between agar concentration and surface motility in *E. coli* [8]. There is a very fine range of agar concentration over which *E. coli* are capable of swarming (0.45% - 0.50% w/v) [11]. The current thinking in the field is that this dependence can be attributed to the change in viscous drag associated with changing agar concentrations. However, it is not known how the viscous forces that act on bacteria near the agar surface vary with agar concentrations. By accurately measuring the diffusion of moving objects close to agar surfaces, it is possible to estimate the viscous drag to explain the highly sensitive dependence of swarming on agar concentrations.

The diffusion of probe colloidal particles provides quantitative information about the viscous drag in various environments. A freely moving self-diffusive sphere with radius a, suspended in a viscous fluid with viscosity η, and with a velocity $\boldsymbol{U}$, experiences an opposing drag force $\boldsymbol{F}$ that is given by Stokes Law:

$$\boldsymbol{F}_0 = -6\pi\eta a\boldsymbol{U}$$

This relationship applies in the low Reynolds number regime (where viscous forces dominate over inertial forces). The diffusion coefficient of the sphere, D_0, is given by the Stokes-Einstein relation:

$$D_0 = \frac{k_B T}{6\pi\eta a}$$

where k_B is the Boltzmann constant and T is the temperature.

Close to a solid surface, the no-slip boundary condition typically applies. The fluid layer close to the surface has zero velocity and no mass flux is possible through that the

surface. As a consequence, the viscous drag experienced by a probe bead become increasingly large as the distance between the surface and the probe decreases. This in turn reduces the bead's diffusivity close to the surface [96]. However, if the bounding surface is a porous gel, the no-slip condition is not entirely valid and partial-slip may occur at the bounding surface. Additionally, the gel being porous, mass flux is not zero at the bounding surface. Thus, we expect the viscous drag near agar surfaces to be lower compared to solid, no-slip boundaries [97-100]. In this chapter, we will measure the diffusion of a spherical particle close to agar surfaces to determine how the viscous drag varies with agar concentrations.

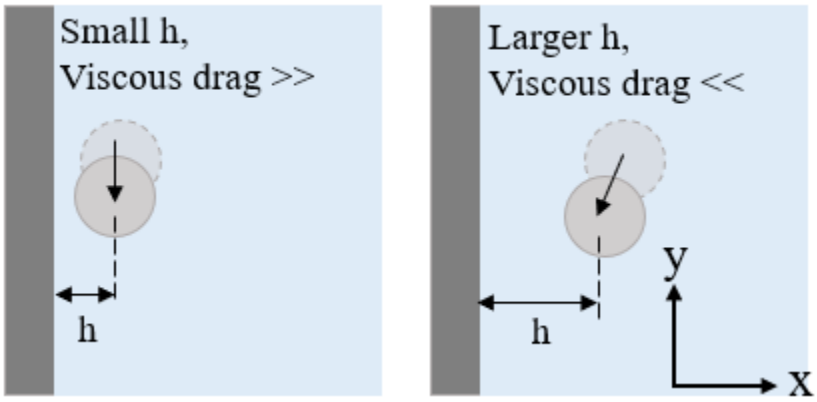

Figure 3-1 Schematic of a diffusing particle near a solid, no-slip boundary, viewed from the side. When the particle is close to the boundary, viscous drag increases and the diffusion is dampened. As the particle moves away from the boundary, viscous drag decreases and diffusion of the beads increases. The x-direction, normal to the surface, is referred to as the transverse mode and the y-direction, parallel to the surface, is referred to as the lateral mode.

The effect of the solid boundary on the diffusion of a particle has been theoretically modeled by Lorentz and Faxen [101, 102]. Brenner *et al*. provided refined expressions for the dependence of lateral and transverse diffusion of a spherical particle on the separation

distance from a rigid wall, see Figure 3-1 [103-105]. The cogency of such theoretical predictions has been successfully tested and validated by various experimental approaches including photonic force microscopy [106], optical trap microscopy [107, 108], near-wall velocimetry [109] , three-dimensional total internal reflection velocimetry (TIRV) [110], three-dimensional ratiometric total internal reflection fluorescence microscopy (3-D R-TIRFM) [111], standard and multilayer nano-PIV [112], and different dynamic light scattering (DLS) approaches such as standard DLS [113] , low-coherence DLS [114], resonance-enhanced DLS [115] , and evanescent wave DLS [116, 117].

One limitation of the aforementioned experimental approaches is the inability to precisely measure the separation distance of the particle from the surface of interest. Many approaches employ a 2D top view where the bounding surface is parallel to the focal plane. In such a set-up, direct measurements of particle separation are difficult to make and often rely on estimates of the separation distance [108]. In a recent advance, a vertical imaging chamber which orients a bounding surface perpendicular to the focal plane was developed [118]. Here, we take advantage of this innovation to accurately measure the diffusion of single latex beads as a function of the separation from solid (glass) and soft (agar) surfaces. We measured diffusion of the beads across a range of separation distances to indirectly determine the surface drag at different agar concentrations. We then analyzed the changes in diffusion to estimate the surface drag near soft-substrates. We found that across a range of agar concentrations, agar behaves in a manner that is unexpectedly similar to a no-slip surface.

3.2 Materials and Methods

3.2.1 Media

Media consisted of either Eiken Agar or Bacteriological Agar (Amresco) and millipore water (Millipore Milli-Q Synthesis). The media was autoclaved and maintained at 65°C for up to 5 days before use. After 5 days, media was discarded and fresh media was made.

3.2.2 Vertical Imaging Chamber

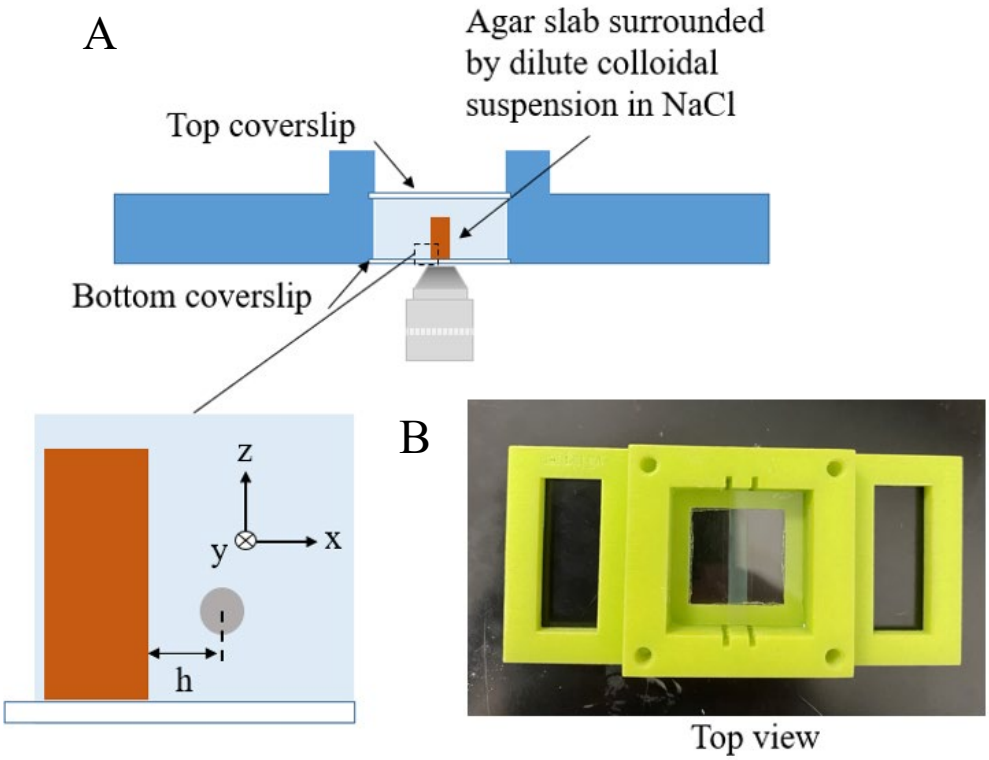

Figure 3-2: Vertical imaging chamber drawings. A) Schematic of the custom imaging chamber showing the orientation of the agar surface perpendicular to the focal plane. B) A top-view of the closed system

A custom vertical imaging chamber was designed to enable orientation of the agar surface perpendicular to the focal plane [118], see Figure 3-2. A 22mm x 22mm coverslip (VWR) was glued on to the bottom of the chamber with RTV108 translucent adhesive (Momentive). We let the adhesive cure for 24 hours and then checked the chamber for leaks prior to use.

Two cut glass microscope slides were placed in the chamber as shown in Figure 3-3. A custom 3D-printed lid was then placed on the chamber, seated on the cut glass slides, and secured with M3 screws to achieve the smallest possible gap between the cut glass slides and the coverslip on the bottom of the chamber. The lid helped to minimize agar leakage. 250 µl of molten agar was poured between the cut glass slides and allowed to cure for 20 minutes prior to removal of the lid. The agar slab was self-supporting once the lid and glass were removed. Once the agar was cured and the glass slides were removed, a dilute suspension of 2 µm diameter polystyrene beads (Cat# 19814, Polysciences Inc.) was introduced to the chamber and a coverslip was placed on top of the agar and suspension to close the system, as shown above in Figure 3-2.

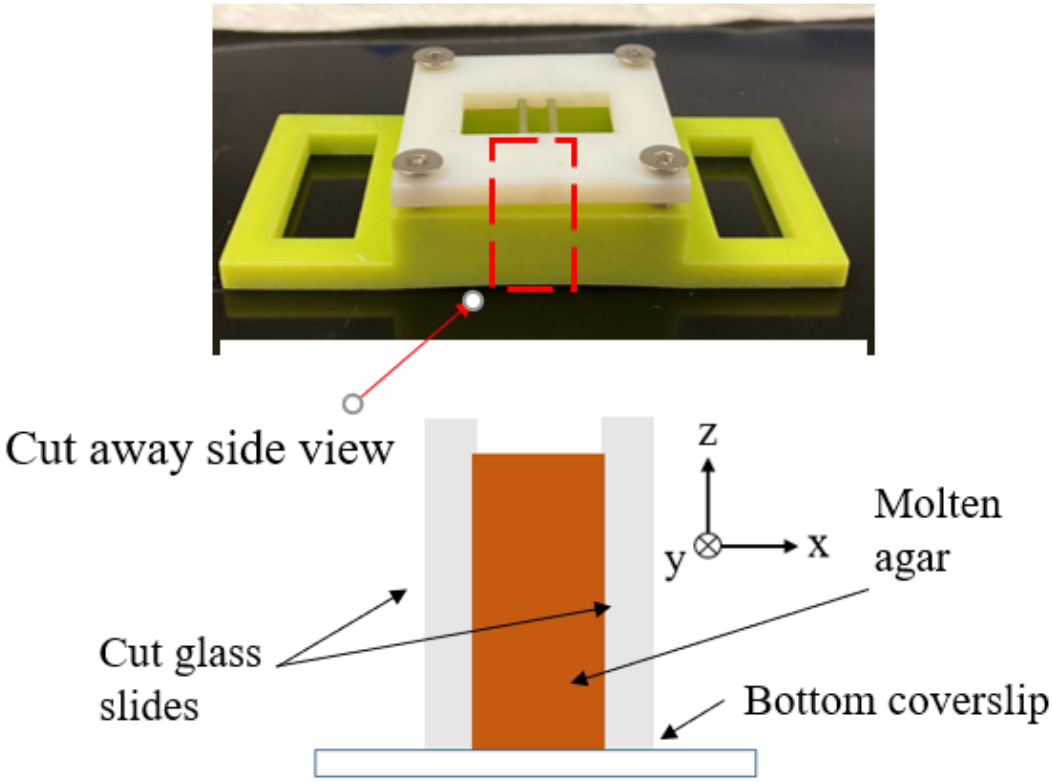

Figure 3-3 Molten agar pouring schematic. This schematic depicts how the agar slab was poured, using cut glass microscope slides as supports during cooling to orient the slab perpendicular to the focal plane.

3.2.3 Blinking Optical Tweezers

The optical traps were generated with a laser of wavelength of 976 nm (CW, 10W, Azur Light Systems, ALS-IR-132) at 0.51W power. The laser beam was directed in to the back aperture of a Nikon Eclipse Ti microscope with a high N.A. water immersion objective (60X, N.A.1.2), bringing the beam into a tight focus at the focal plane of the microscope [119]. The focused beam creates a strong electric field gradient which attracts dielectric particles to the point of greatest intensity (the waist of the beam, or, the narrowest point of focus). We introduced an optical chopper wheel in the optical path

(ThorLabs Optical System-MC2000; chopper wheel MCF1F2) which rotated at a frequency of 8Hz to generate blinking traps. The duration between two laser 'on' events was ~0.125 s, during which the bead diffused. The Nikon Eclipse Ti served as both the imaging and optical trapping system. Videos were recorded using uEye cockpit at 80 fps (UI-3240LE-M-GL, IDS Imaging Development Systems GmbH).

3.2.4 Data Analysis

Each video captured ~150 trajectories for a single particle for a given separation distance. A single trajectory encompassed the displacement of the bead between two laser "on" events. Approximately 10 frames were captured in between each laser "on" event and the first six frames were used to determine single trajectories. The effect of gravity is weak and can be ignored at such short-time scales. Videos of particles were analyzed with custom written MATLAB codes based on a standard approach to determine the mean-squared-displacement (MSD) of the center of the bead between frames [120, 121].

If $\vec{r}$ is the position vector of the center of the bead, then the total MSD, ($<\Delta r^2>$) is:

$$< \Delta r^2 > = < \Delta x^2 > + < \Delta y^2 >$$

where $<\Delta x^2>$ and $<\Delta y^2>$ are the mean-squared-displacement in the x and y axis, respectively. The transverse and lateral diffusion modes are oriented along X and Y, respectively. The diffusion coefficient was calculated from the MSD using the following equation:

$$MSD = 4D\tau^{\alpha}$$

where D is the diffusion coefficient, τ is the lag time, and α is the diffusion exponent (α =1 in Newtonian fluids). The diffusion coefficients along the modes were calculated from

the slopes in the respective MSD plots. The α for each MSD plot was found by fitting the slope of the log plot. This value was checked for every particle analyzed to ensure the system was not super-diffusive or sub-diffusive, especially close to the agar.

Experimental values were compared to theoretical models from the literature. The transverse diffusion coefficient was modeled using Brenner's solution of the Navier-Stokes equation for a creeping flow with boundary conditions derived to correct for near-wall impacts on normal Brownian motion [103, 122]:

$$\frac{D_\perp}{D_0} = \frac{4sinh\alpha^B}{3}\sum_{n=1}^{\infty}\frac{n(n+1)}{(2n-1)(2n+3)} \times \left[\frac{2\sinh(2n+1)\alpha^B + (2n+1)sinh2\alpha^B}{4sinh^2\left(n+\frac{1}{2}\right)\alpha^B - (2n+1)^2sinh^2\alpha^B} - 1\right]$$

where $\alpha^B = \cosh^{-1}\left(\frac{h}{R}\right)$, R is the radius of the sphere, h is the distance of the center of the sphere from the surface, $D_\perp$ is the diffusion coefficient perpendicular to the surface, and D_0 is the bulk diffusion coefficient. The diffusion coefficient in the lateral mode was calculated using Faxen's model [123]:

$$\frac{D_\parallel}{D_0} \approx 1 - \frac{9}{16}\frac{R}{h}$$

where $D_\parallel$ is the diffusion coefficient in the direction parallel to the surface.

3.2.5 Separation Distance Measurements

ImageJ software [124] was used to manually draw a straight line from the center of the bead to the agar surface, which was visible across all agar concentrations. This line was measured in pixels and converted to microns based off of a known scale factor. To determine the average error associated with separation distance measurements, one

measurement was repeated three times and the standard error of the measurements was calculated.

3.3 Results

3.3.1 Bulk diffusion measurements

First, we measured diffusion of beads in the bulk fluid, far away from any surfaces. Diffusion coefficients were calculated from the slope of the MSD plot. Bulk diffusion was recorded at various timepoints throughout each experiment. For each video ~100-150 trajectories were recorded at a distance > 50 µm from the bounding surface and > 50 µm from the bottom surface of the imaging chamber. Videos were analyzed as described above. The average bulk diffusion coefficient was calculated for both parallel and transverse modes (n = 46 and n =48, respectively). The bulk diffusion data sets were fit to a normal distribution, shown below, and the mean of the normal distribution was used to normalize all data. The mean bulk diffusion coefficient for the parallel mode was 0.226 $\pm$ 0.01 and the mean bulk diffusion coefficient for the transverse mode was 0.218 $\pm$ 0.01.

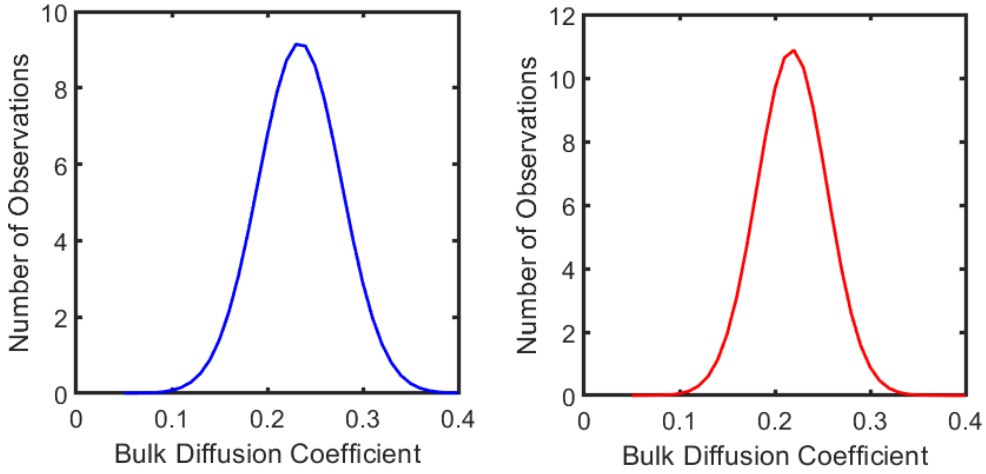

Figure 3-4 Normalized distribution of experimental bulk diffusion coefficients for parallel (blue) and transverse (red) diffusion modes. The mean bulk diffusion coefficient for the parallel mode was $0.226 \pm \mathbf{0.01}$ and the mean bulk diffusion coefficient for the transverse mode was 0.218 ± 0.01.

3.3.2 Diffusion near a no-slip glass boundary

Next, we measured the diffusion of a bead near a glass surface. The MSD vs τ remained linear and there were no observable hydrodynamic flows due to leakages (Figure 3-5A). Diffusion coefficients were calculated from the slope of the MSD plot for each separation and then normalized to an average bulk diffusion coefficient. The bulk diffusion coefficient was measured as described previously. The dependence of diffusion on separation for the two modes is shown in Figure 3-5B. The parallel (blue squares) and transverse (red circles) measurements agreed with predictions based on theoretical models discussed previously.

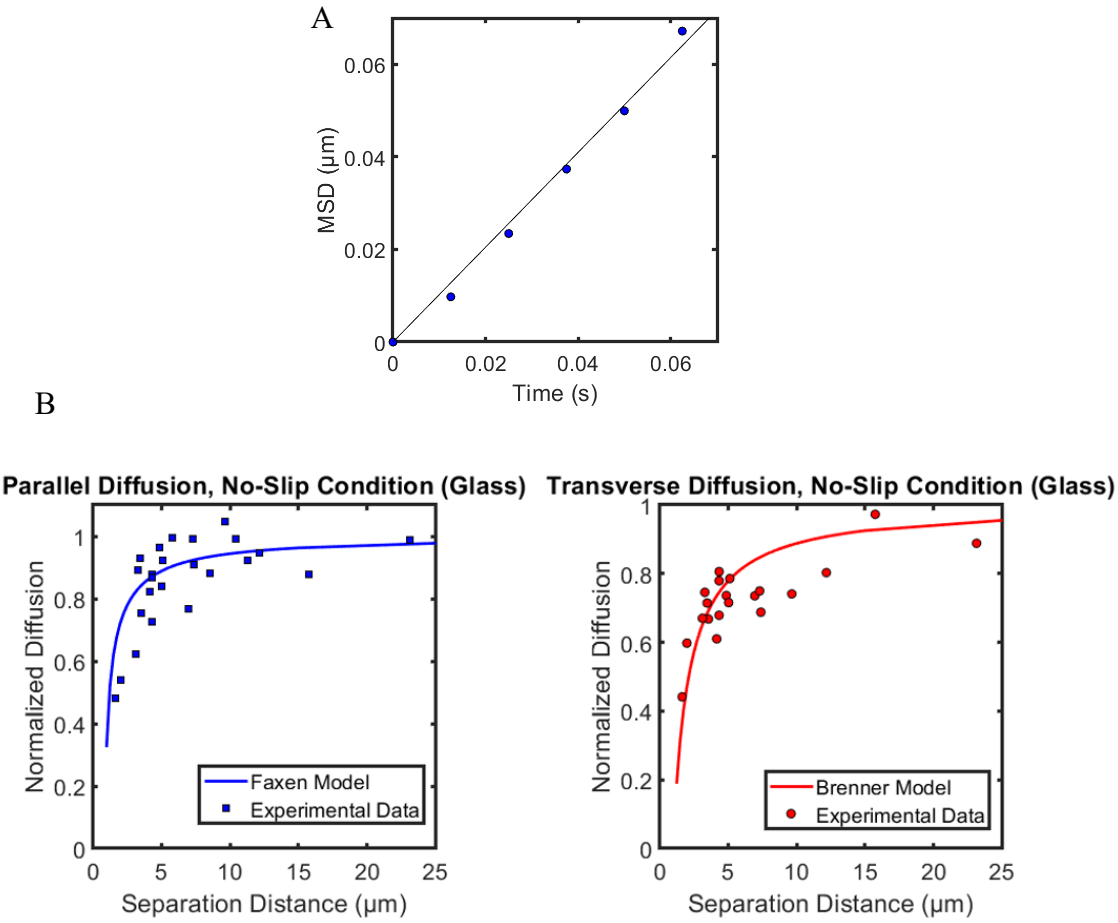

Figure 3-5: Mean-squared-displacement plot and diffusion coefficient for a no-slip wall A) The MSD vs τ plot is used to calculate the diffusion coefficient for a bead. B) Diffusion coefficient as a function of separation distance from a no-slip glass surface for the parallel and transverse modes. The experimental data is shown by blue squares and red circles for the parallel and transverse components respectively. The theoretical predictions for a no-slip boundary are indicated by the solid curves (blue: Faxen's model, red: Brenner's model).

3.3.3 Diffusion near agar boundaries

We measured diffusion at discrete separation distances from agar surfaces across a range of agar concentrations for both Bacto agar and Eiken agar(see Materials and Methods). Figure 3-6 shows a representative experimental view of a bead, viewed from

below, near an agar surface. The agar surface was visible as a dark blurred line but the exact edge of the surface was not discernable. After the data was recorded, we recorded a second video where the bead was dragged into the agar surface to locate the exact edge. This was used to determine a more precise separation distance between the bead and the wall.

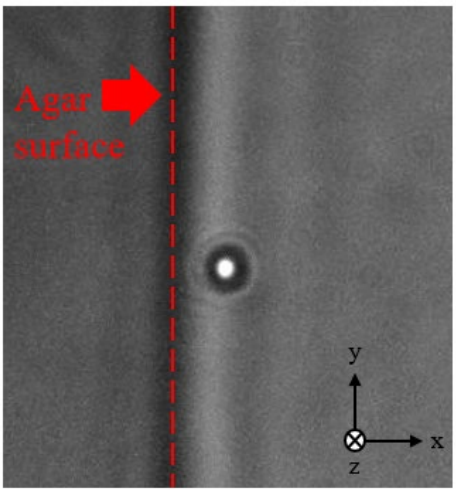

Figure 3-6: Experimental view of diffusing bead near an agar surface.

Figure 3-7 shows the experimental data for Bacto Agar plotted against the theoretical models. The parallel mode data is represented by blue squares and the transverse mode data is represented by red circles. Our results show the asymmetry between the parallel and perpendicular diffusion, as was expected based on theoretical predictions. The experimental data also seems to agree relatively well with the theoretical predictions for a no-slip condition. The sample sizes for each data set are given below in Table 3-1. It is important to note that the parallel and transverse trajectories were treated independently of one another. At low Reynolds number regimes, where viscous forces

greatly outweigh inertial forces, the diffusion of a bead is instantaneous and, thus, has no time or history dependence.

Table 3-1: Sample sizes for Parallel and Transverse diffusion modes for Bacto agar

Agar Concentration	Parallel Mode	Transverse Mode
0.45%	n = 27	n = 27
1.0%	n = 25	n = 28
2.0%	n = 28	n = 31
3.0%	n = 30	n = 29
4.0%	n = 31	n = 29

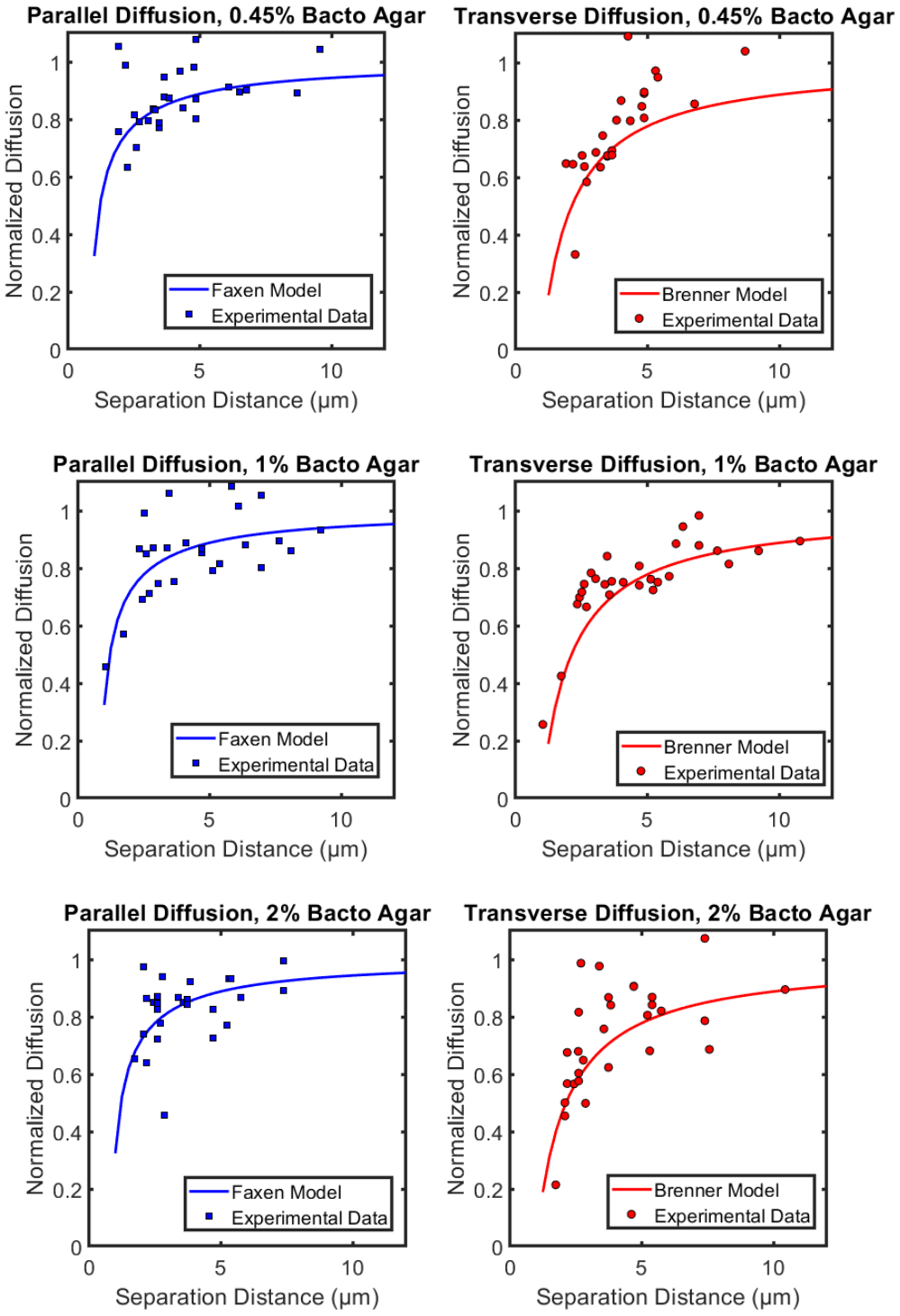
Parallel Diffusion, 0.45% Bacto Agar
Transverse Diffusion, 0.45% Bacto Agar
Parallel Diffusion, 1% Bacto Agar
Transverse Diffusion, 1% Bacto Agar
Parallel Diffusion, 2% Bacto Agar
Transverse Diffusion, 2% Bacto Agar
Normalized Diffusion
Separation Distance (μm)
Faxen Model
Brenner Model
Experimental Data
0
0.2
0.4
0.6
0.8
1
0
5
10

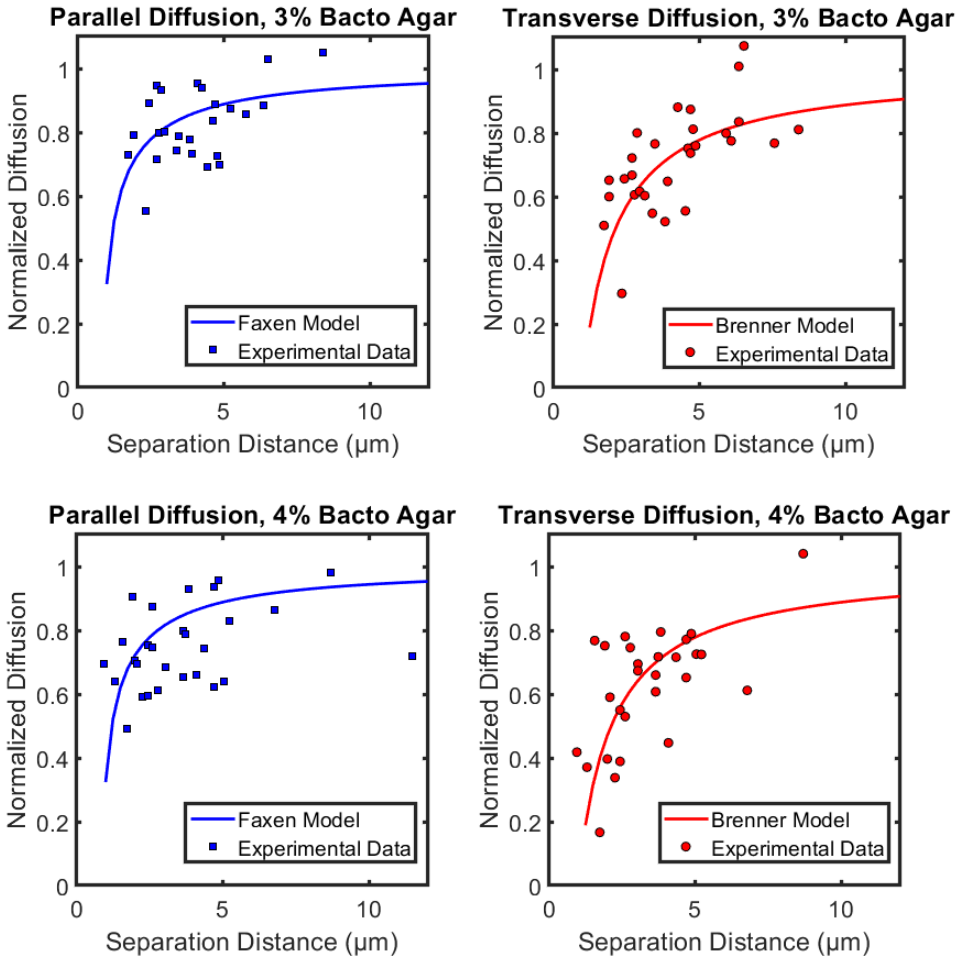

Figure 3-7: Diffusion coefficient as a function of separation across a range of Bacto Agar concentrations.

We next examined the relationship between diffusion and separation distance for Eiken agar. Given the peculiar ability of *E. coli* to swarm only on Eiken agar, we hypothesized that diffusion might be greater for Eiken agar compared to Bacto agar. Figure 3-7 shows the experimental data plotted against the theoretical models. Again, parallel mode data is represented by blue squares and the transverse mode data is represented by red circles. The experimental data shows relative agreement with the

theoretical predictions for a no-slip condition. Each agar concentration tested was in relative agreement with the theoretical models. It is important to note that each data set was normalized to the same average bulk diffusion coefficient. Keeping this in mind, we can see that there are no drastic changes in normalized diffusion for 0.45% w/v agar surface compared to the 4% w/v agar surface, or across the entire range of concentrations tested.

Table 3-2: Sample sizes for Parallel and Transverse diffusion modes for Eiken agar

Agar Concentration	Parallel Mode	Transverse Mode
0.45%	n = 27	n = 26
1.0%	n = 29	n = 28
2.0%	n = 29	n = 29
3.0%	n = 26	n = 29
4.0%	n = 25	n = 24

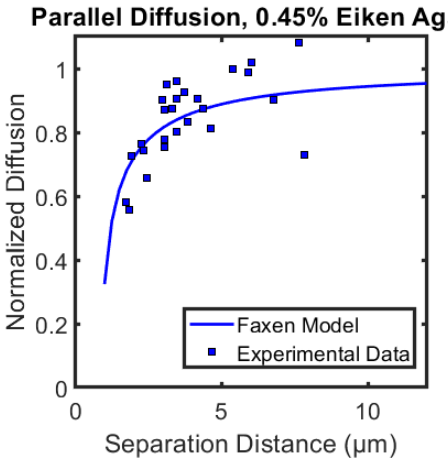
Parallel Diffusion, 0.45% Eiken Agar
Normalized Diffusion
Separation Distance (μm)
Faxen Model
Experimental Data

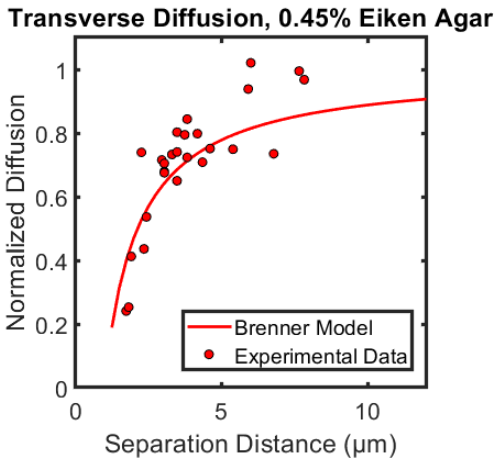
Transverse Diffusion, 0.45% Eiken Agar
Normalized Diffusion
Separation Distance (μm)
Brenner Model
Experimental Data

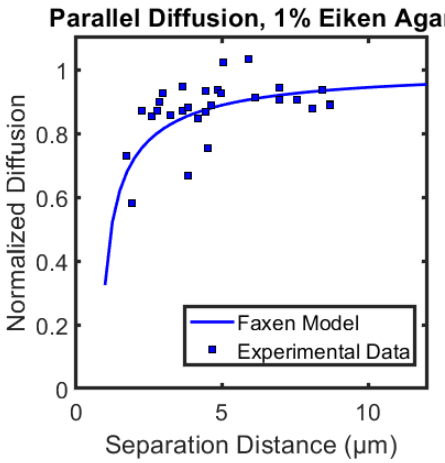
Parallel Diffusion, 1% Eiken Agar
Normalized Diffusion
Separation Distance (μm)
Faxen Model
Experimental Data

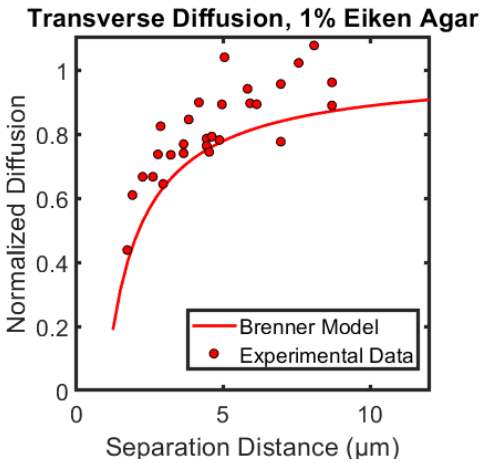
Transverse Diffusion, 1% Eiken Agar
Normalized Diffusion
Separation Distance (μm)
Brenner Model
Experimental Data

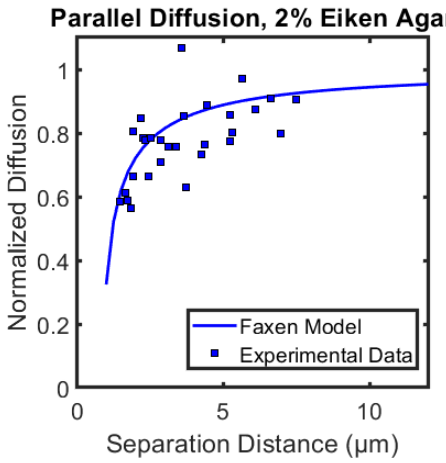
Parallel Diffusion, 2% Eiken Agar
Normalized Diffusion
Separation Distance (μm)
Faxen Model
Experimental Data

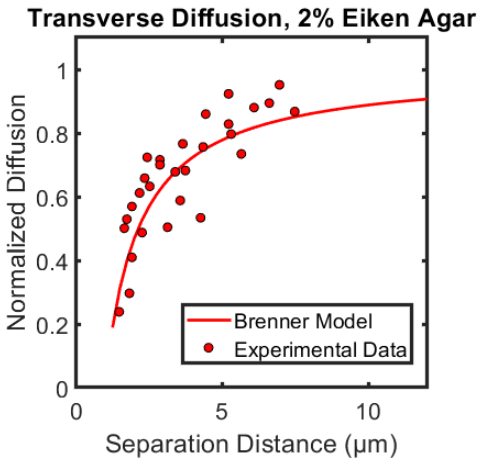
Transverse Diffusion, 2% Eiken Agar
Normalized Diffusion
Separation Distance (μm)
Brenner Model
Experimental Data

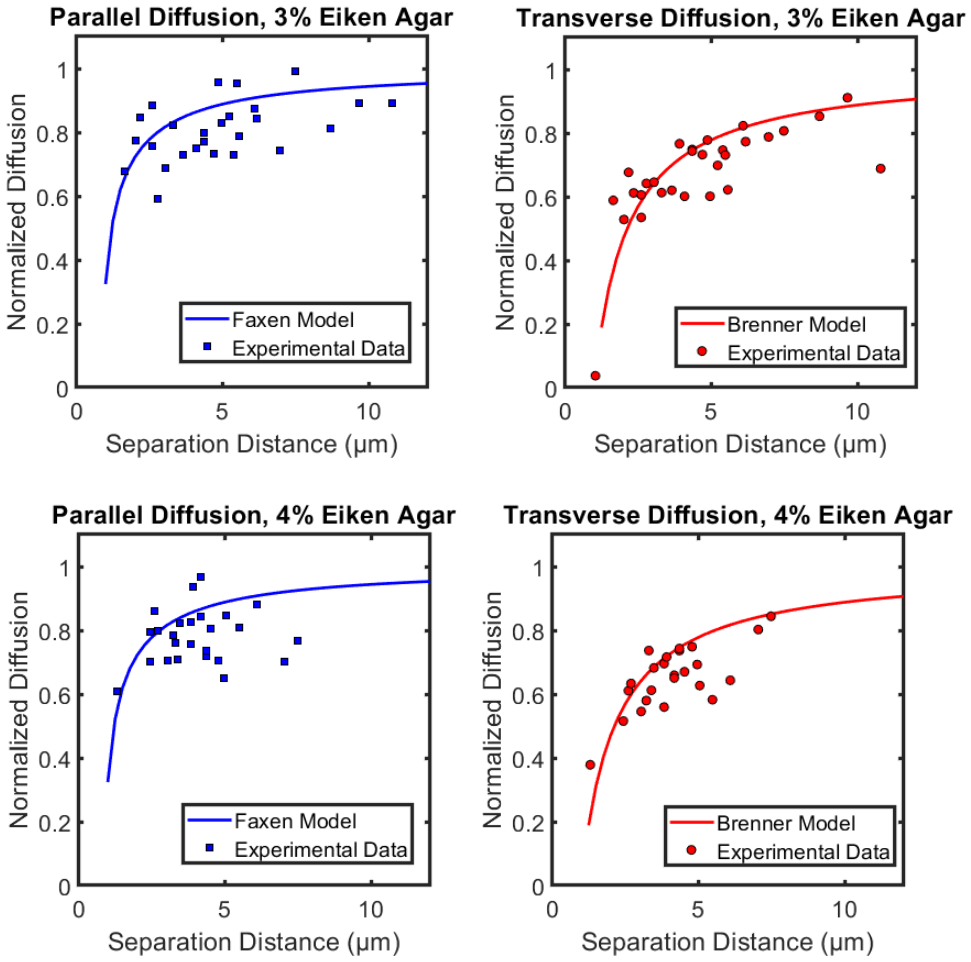

Figure 3-8: Diffusion coefficient as a function of separation across a range of Eiken Agar concentrations.

3.3.4 Diffusion as a function of agar concentration

Finally, we examined the relationship between the normalized diffusion coefficient and agar concentration. We took an average of normalized diffusion coefficients at similar separation distances for each percentage of agar that was examined and plotted the relationship to determine if the diffusion coefficient decreased with increasing agar concentration, as this would be indicative of increased surface drag. Figures 3-9 and 3-10 show the normalized diffusion coefficients as a function of agar

concentration for Bacto agar and Eiken agar, respectively. The data suggests there is a weak relationship between diffusion and agar concentration for Bacto agar and no correlation between diffusion and agar concentration for Eiken agar.

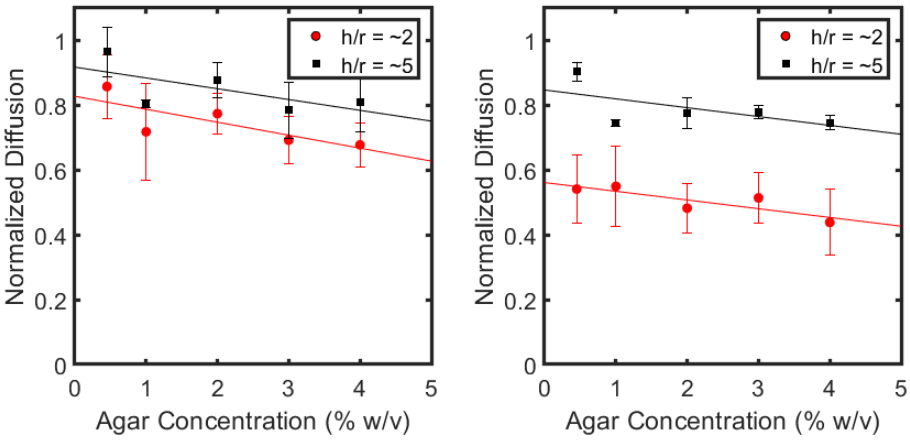

Figure 3-9 Normalized diffusion coefficient as a function of Bacto agar concentration. Parallel Diffusion (left), Transverse diffusion (right)

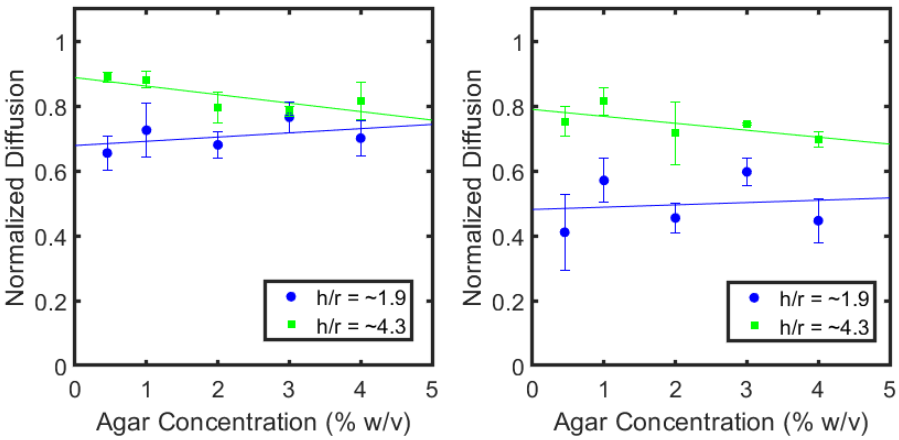

Figure 3-10 Normalized diffusion coefficient as a function of Eiken agar concentration. Parallel Diffusion (left), Transverse Diffusion (right)

3.4 Discussion

For soft surfaces, such as agar, the no-slip condition is unlikely to apply given the porosity of the material. Previous work demonstrated there are appreciable differences in pore size across varying concentrations of agar, see Figure 3-11 [26]. The mechanical properties of agar are heavily influenced by pore size and we hypothesized that the larger pore sizes associated with lower agar concentrations will result in lower surface drag. As pore size decreases with increasing agar concentrations, we expected that the surface drag would increase with agar concentration. However, we found that even 0.45% agar offered similar resistance to diffusion as a solid glass surface. The pore size for 0.5% agar ranges from 500-1200 nm; thus, it is likely that the pore size is about half the size of the bead and lower, which may explain the unexpectedly high surface drag. Also, measurements of the pore size variation with Eiken agar concentration are not currently available in the literature and may be different from the values reported here.

Our results show that the agar surface mimics a no-slip boundary condition, and that surface drag does not vary significantly with agar concentrations over the range of 0.45 – 4% w/v for Eiken agar. This suggests that the sensitivity of *E. coli* to small changes in the agar concentrations is likely not due to changes in the viscous drag near the surface. We speculate that flagella may become entangled within the pores of the agar surface, preventing swarming. The mechanism of switching directions of rotation of the flagella may, in turn, permit disentanglement. Viscous drag for bacteriological agar exhibited a weak dependence on agar concentration which could mean that the pore size of bacteriological agar varies with agar concentration. If the pore size of the bacteriological

agar does indeed vary and is larger than the pore size of Eiken agar, the entanglement theory would explain why *E. coli* fail to swarm on bacteriological agar but not Eiken agar.

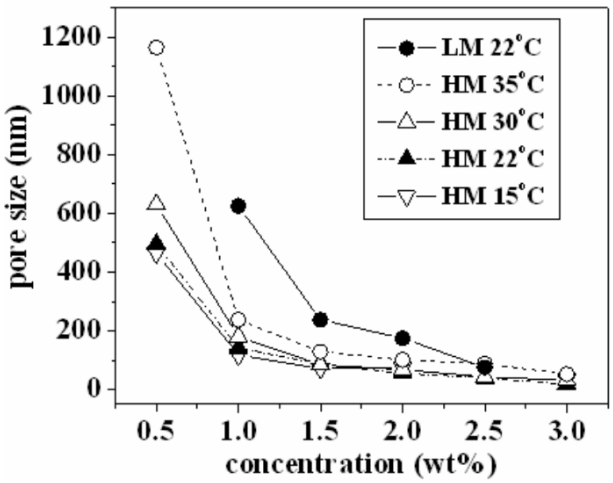

Figure 3-11: Pore size variance vs agar concentration. Pore size variance as a function of agar concentration for high melting point (HM) and low melting point (LM) agars for different setting temperatures [26].

4. DESIGN OF A STICKY FLJK ALLELE FOR BIOPHYSICAL ASSAYS IN *CAULOBACTER CRESCENTUS*

4.1 Introduction

The role of the bacterial flagellar motor (BFM) in motility and virulence, as discussed in Chapter 2, has led to an enormous effort by the scientific community to understand how the BFM functions. The tethered cell assay, first utilized by Silverman and Simon, made use of a polyhook mutant and anti-hook antibodies to tether flagellar hooks in *E. coli* to a glass substrate [125]. This assay allowed researchers to study the flagellar motor response to environmental stimuli and large viscous loads [126-129]. An improvement upon this assay was made when the bead assay was developed to study the response of motors to varying viscous loads. In this assay, a sticky *fliC* allele was utilized to attach polystyrene beads to flagellar stubs [87]. The sticky *fliC* allele was developed by chance through random deletions in a study concerning flagellum antigenicity in *E. coli* [130]. The mutant flagellin, which lacks 57 central amino acids, was first used by the Berg group and reported as $FliC^{St}$ [79]. Later, Yamahuchi *et al*. independently developed a sticky *fliC* allele in *Salmonella typhimurium* after identifying a mutant which retained its ability to swim in the presence of anti-filament antibodies. The mutant harbored deletions in the D3 domain of the flagellin gene [131]. This mutant was reported as *fliC* Δ(205-293) in a later work where it was utilized for bead assays [132] and is shown below in Figure 4-1A. The sticky *fliC* allele is now widely used in motor characterization studies, as it allows high throughput tethering of cells or beads for biophysical characterization [49, 52, 80, 133-135]. The discoveries that have resulted from the implementation of the sticky

fliC allele have been numerous, but limited to the species in which the alleles were discovered.

Recently, the sticky *fliC* allele from *S. typhimurium* was successfully combined with the hag gene in *Bacillus subtilis* to create a sticky chimera. The D2 domain (142-203 and 293-395) of *Salmonella* FliC Δ(204-292) was flanked by the N-terminal and C-terminal segments of *hag*, respectively [51]. The chimeric DNA is shown below in Figure 4-1B. The work utilizing this sticky chimera was the first of its kind for the species, examining the torque-speed relationship over a wide range of loads, and provided valuable insights into the dynamics of the stators in the flagellar motor of *B. subtilis*. Extension of such sticky chimeric DNA to other species, such as *Caulobacter crescentus*, would help address open questions in the field. There are many open questions concerning *C. crescentus*, among other species, and the mechanism it uses to sense surfaces. A functional, sticky flagella would allow probing of the motor under various loads and could provide valuable insights into the pathways which trigger irreversible attachment to surfaces.

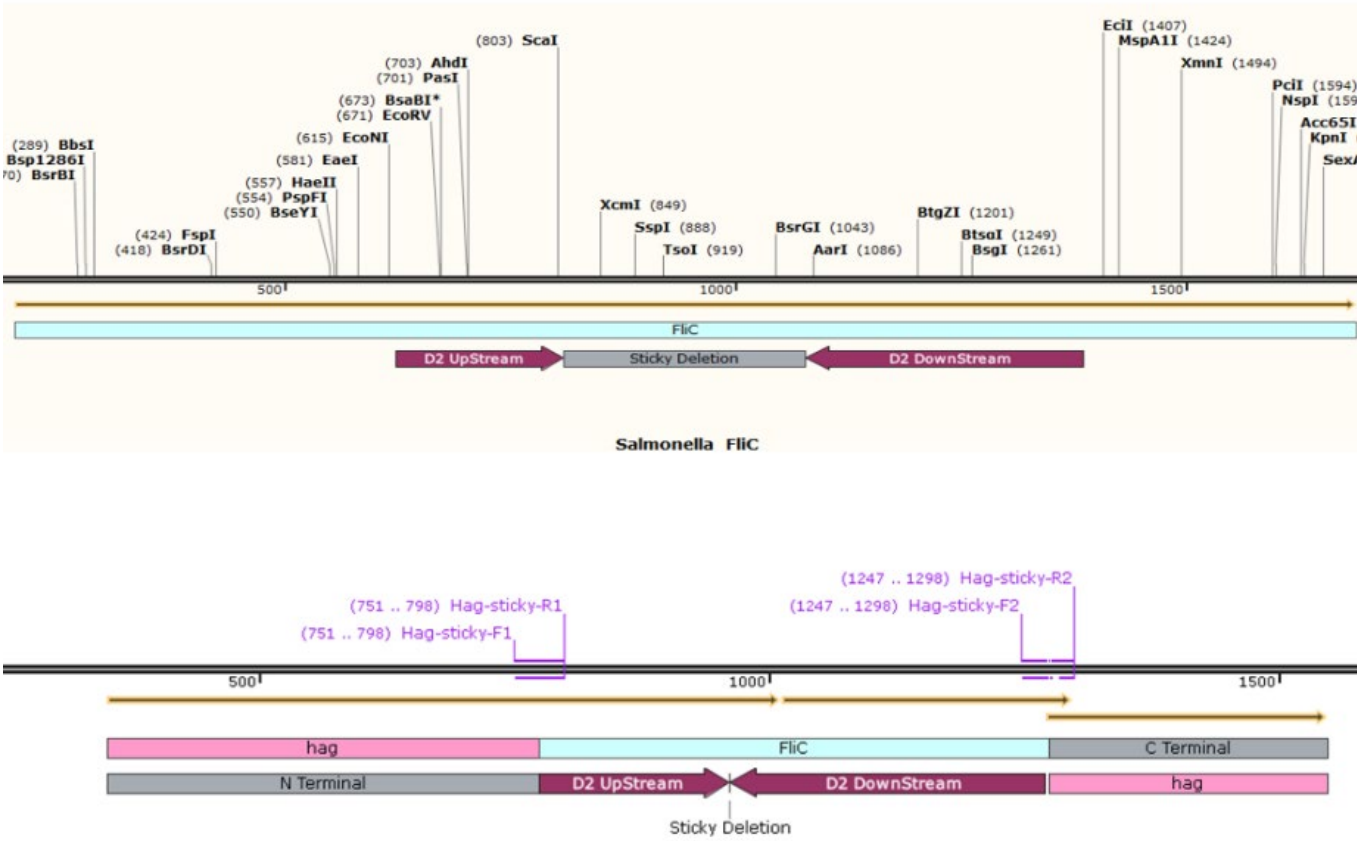

Figure 4-1: Visual representation of the design of the sticky hag chimera. The top figure shows the block diagram of the genetic sequence for *fliC* in *Salmonella*, with the grey region denoting the portion of the gene that when deleted, renders the protein sticky. The bottom figure shows the block diagram for the genetic sequence of the hag chimera which contains the D2 region of *Salmonella fliC* sans the deleted portion, as denoted in the top figure.

4.2 Goals

The goal of this project was to design a sticky *fljK* chimera for use in *Caulobacter crescentus.* The sticky *fliC* allele in *S. typhimurium* was used, as the D2 domain had already been identified as sufficient for creating a sticky allele elsewhere [136]. Despite recent efforts by our lab, which will be discussed in the results section, we were unable to identify the portion of the $FliC^{St}$ mutant which is responsible for sticking to glass surfaces.

We compared sequence homology between *fljK* and *fliC* to determine conserved domains and target the non-conserved portions of the sequence to make deletions and insertions of the D2 domain, or portions of the D2 domain. Using molecular simulations programs such as SWISS-MODEL [137] and CHARMM (Chemistry at HARvard Macromolecular Mechanics) [138], we predicted how the deletions and insertions will alter the protein folding. This allowed us to avoid making deletions that resulted in non-native folding that would likely inhibit function of the protein. We targeted hydrophobic amino acid residues for insertions and attempted to insert them such that they were surface exposed to allow for tethering to glass substrates. Once these constructs were thoroughly investigated via modeling, they were expressed in a Δ*fljK* strain via an inducible plasmid for functionality.

4.3 Methods

4.3.1 Bacterial Strains and Plasmids

The sticky D2 domain of *fliC* was amplified via PCR from strain BD8571, a *B. subtilis* strain harboring the sticky *hag* chimera. This strain was a gift from David Dubnau. Overlap PCR was used to create the chimeric DNA, carrying N-terminal and C-terminal domains of *fljK* and the D2 domain of *fliC.* Once the chimeric DNA was constructed, it was confirmed via sequencing (Eurofins Genomics) and inserted into a plasmid inducible by xylose, pBXMCS2 [139], via restriction digest and ligation. Protocols for restriction digest and ligation are included in Appendix B. The plasmid harboring the chimeric DNA was then transformed, via electroporation, into TPA1254 a ΔJKLMNO strain [140].

4.3.2 Motility Assays

To test for motility of strains harboring the sticky plasmids, day cultures were grown in PYE and induced with 0.8 M Xylose and 5 μg/mL Kanamycin, as was reported elsewhere [141]. Planktonic cells were diluted in either fresh PYE (1:10 dilution) or suspended in motility buffer. The dilute suspension was observed in a standard flowcell and cell-motion away from either surface (coverslip or microscope slide) was recorded at ~60 fps with a CCD camera (DCC1545M-GL, Thorlabs Inc).

4.3.3 Protein BLAST

Sequences for the genes of interest, *S. tyhpimuirum fliC* and *C. Crescentus fljK* were obtained from the online database BioCyc [139]. Protein BLAST (Basic Local Alignment Search Tool) was then used to align the sequences to find homology between the two genes [142].

4.3.4 SWISS-MODEL

SWISS-MODEL, an online automated protein structure homology-modeling server was used to predict protein structures [137].

4.3.5 Error-Prone PCR

A standard error-prone PCR technique was used based on published methods [143]. Taq polymerase was used because of its naturally high error rate. The estimated error rate for the reaction was 1-2 bp per 1 kb. This protocol is outline in Appendix B.

4.4 Results

4.4.1 Model based amino acid deletions

Four sticky chimera constructs were initially designed and tested based on sequence homology between *fljK* and *fliC (Salmonella)*. The N-terminal and C-terminal regions of *fljK* were retained based on high alignment scores between the two proteins, which were identified using P-BLAST, alignment scores are shown in Figure 4-2 and a detailed report of the alignment is given in Appendix C.

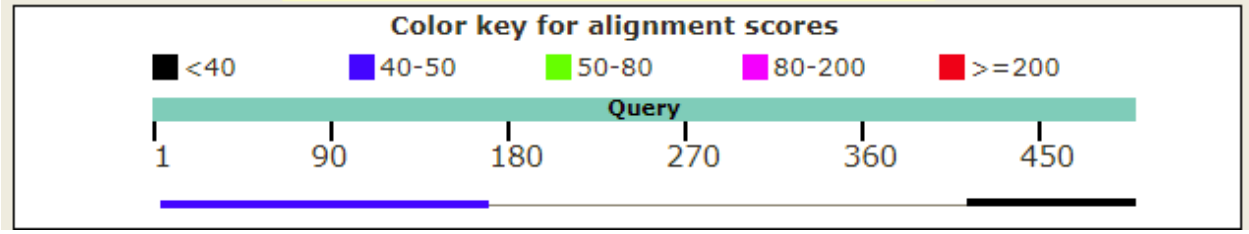

Figure 4-2: Protein Blast for fljK and fliC (query)

Figure 4-3 (left) shows the SWISS-MODEL cartoon structure for *fljK* based on 25.97% sequence identity match with a crystal structure of a bacterial cell-surface flagellin from *Sphingomonas.* A detailed report of the modeling quality and parameters is given in Appendix 4. Figure 4-3 (right) shows a Van der Waals representation of the protein *fljK* with the N and C terminal regions of the protein shown in red and blue, respectively. As stated previously, various sections of *fljK* which did not show high alignment scores with *fliC* (high alignment scores were interpreted as highly conserved sequences, which likely indicates portions of the gene that must be retained) were replaced with the D2 domain of the sticky *fliC* allele from *S. typhimurium.*

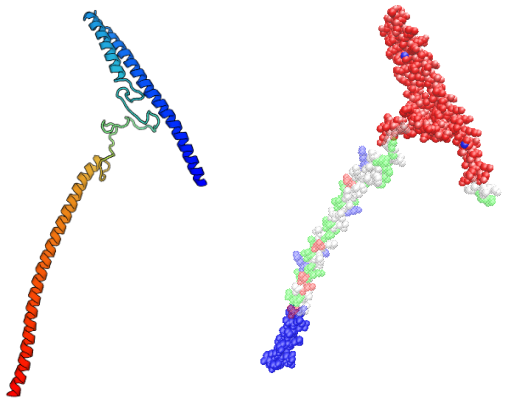

Figure 4-3 *SWISS-MODEL* structure of *fljK (left)* and Van der Waals surface representation (right) identifying N-terminal (red) and C-terminal (blue) regions.

Initial constructs were designed based only on sequence alignment and had the following individual deletions, respectively: *fljK* Δ(142-172) – referred to as "Sticky A", *fljK* Δ(144-189) – referred to as "Sticky B", and *fljK* Δ(150-171) – referred to as "Sticky C" and in place of these deletions had the D2 domain for sticky *fliC*. The fourth construct had no deletion in *fljK* but simply had the D2 domain of the sticky *fliC* allele inserted at AA150. Constructs were made via overlap PCR as described in the materials and methods and transformed via an inducible plasmid and expressed in the strain previously described. Of the four aforementioned constructs, none were observed to be functional. Figure 4-3 (top) highlights the different fragments of *fljK* which were deleted, respectively. Given that sequence homology was not sufficient to predict which deletions would allow *fljK* to retain functionality, we implemented protein modeling for more accurate modeling. The SWISS-MODEL database was used to predict structures of the various deletions and the PDB coordinates were downloaded and visualized using VMD software [144].

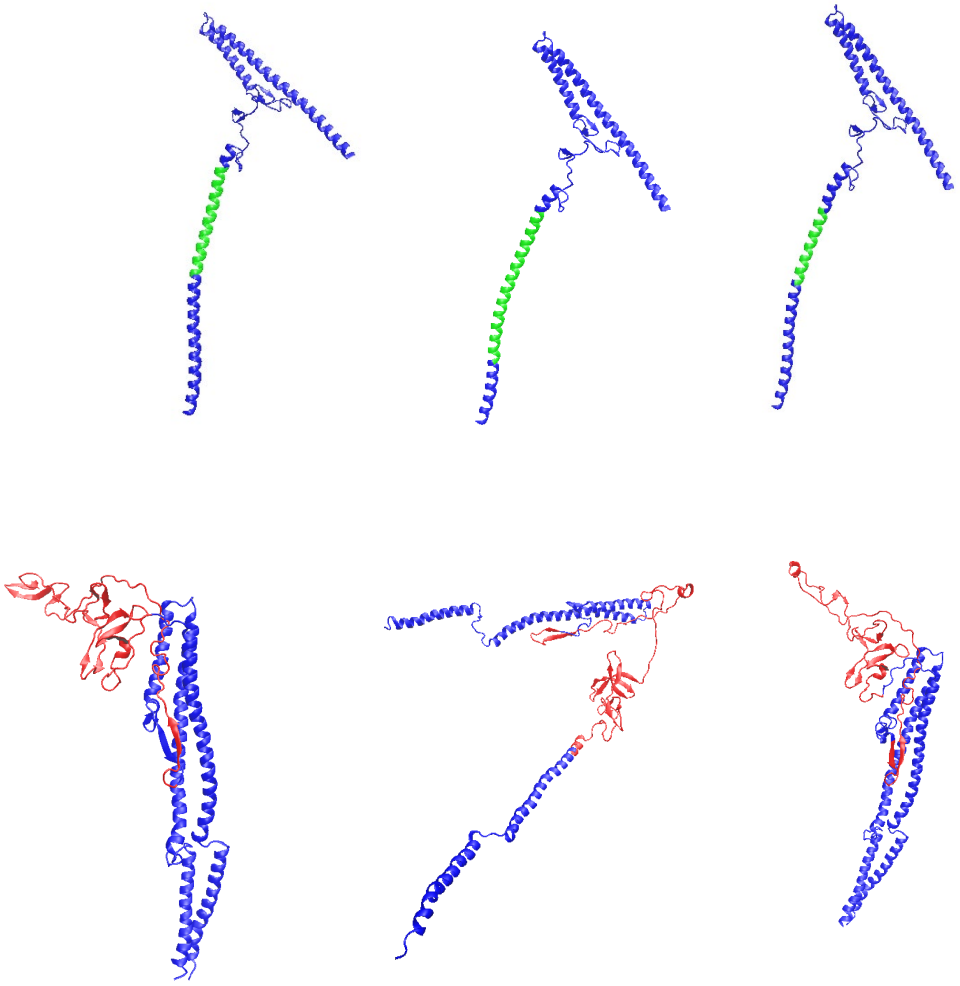

Figure 4-4: Protein visualizations for deletions and sticky insertions with and without modeling. (Top): The structure of fljK showing each of the deletions made in the flagellin portein, respecitvely: fljK Δ(142-172), fljK Δ(144-189), and fljK Δ(150-171). (Bottom): Corresponding SWISS-MODELS for the above deletions and addition of the D2 domain from Salmonella fliC.

The models of the chimeric DNA, shown in Figure 4-4 (bottom) display obvious issues in protein folding between the native *fljK* structure and the designed DNA constructs. This led us to target smaller regions for replacement with hydrophobic

residues, in place of inserting the entire D2 domain, in hopes of minimal disruption to protein folding. Previous work revealed that the 167th amino acid of *fljK* (alanine shown in red), shown in Figure 4-5 (left), was surface exposed, making it suitable for fluorescent labeling purposes. Based off models of FliCSt from *E. coli*, we found that there were two small patches of hydrophobic regions which were surface exposed: L-Y-A-A (residues 327-330) and Y-Y-S-A (residues 332-335). We identified these two patches as potentially being responsible for the stickiness of the protein. These residues are identified in Figure 4-5 (middle) and 45 (right), respectively. Thus, we made three insertion of hydrophobic patches at the 168th amino acid. The three insertions resulted in the following hydrophobic patches: L-L-Y-A-A, L-Y-A-A, and L-Y-Y-S-A. None of the three constructs were functional.

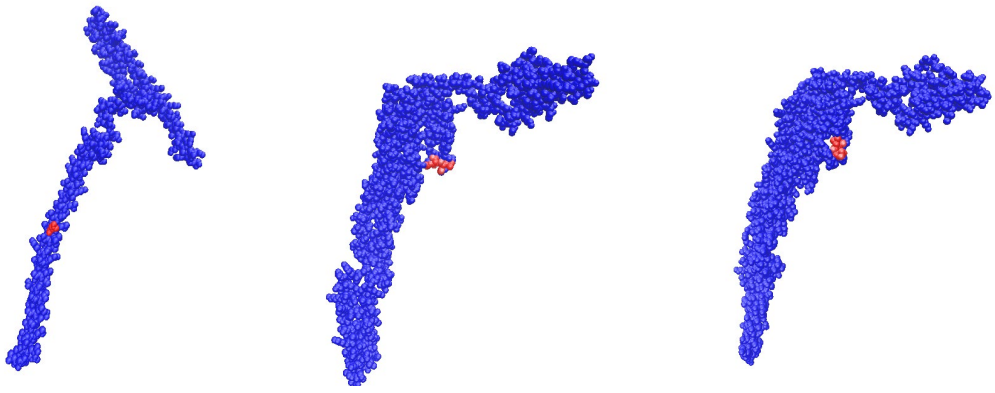

Figure 4-5: Representations of target sequences from *fljK* and *fliC*. Left:The Van der Waals representation of FljK with residue 167 identified in red. Middle: The surface exposed residues from FliCSt 327-330. Right: The surface exposed residues from FliCSt 332-335

4.4.2 Error Prone PCR approach

A standard error-prone PCR approach was used to create mutant libraries of *fljK*. Random mutations were made to the constructs previously described and named "Sticky A", "Sticky B", and "Sticky C". Additionally, random mutagenesis was performed on the construct which contained an L-Y-A insertion between AA166 and AA167. Approximately 125 mutants have been isolated and transformed into plasmids for testing. Many of these mutants remain un-tested. Of the approximately mutants that have been tested (pKMF 1-6), no functional mutants have been identified.

4.5 Future work

Moving forward, we will utilize CHARMM in an attempt to develop more accurate protein models for the sticky *fliC* allele in *Salmonella* as well as $FliC^{St}$ in *E.coli*. These models will provide insights into which residues are becoming surface exposed due to deletions and how the folding of the protein is being altered. Once these residues have been pinpointed and folding changes have been predicted, we can then model various deletions and insertions in *fljK* to try and find a combination which will retain function. Before proceeding with designing new deletions in CHARMM, we will model the deletions which have already been constructed and failed to function properly in order to verify the accuracy of the modeling.

An additional consideration for the sticky constructs that have been created is that they are sticky but unable to generate thrust. This could explain the lack of visible motility. To test to see if the filaments are sticky, we will use the optical tweezers to trap the cells and bring them in contact with the surface of a microscope slide and check for tethering.

5. CONCLUSIONS AND FUTURE WORK

This dissertation describes novel work which characterized the motors of swarming *E. coli*. Previously, such characterization has been carried out with planktonic cells but not cells that have transitioned to a swarming state. This work has expanded the current understanding of how the bacterial flagellar motor of *E. coli* responds to surfaces and surface induced motility. Contrary to previous studies which emphasized the role of switching in swarming, we have presented new evidence which suggests swarming cells have a decreased propensity for motor reversals. We proposed that it is not switching *per se*, but rather some associated property of the wildtype that enables swarming. Additionally, we found evidence that the CW-locked conformation of FliG-FiM-FliN protomers affected flagellar export and that putative motor assemblies were inhibited by agar surfaces.

To further elucidate surface-induced changes observed in *E. coli*, we sought to probe the mechanical environment of swarmers. The hypothesis in the field is that the increased viscous load is responsible for the inhibition of swarming in *E.coli* above 0.5% agar w/v. This hypothesis was untested owing to the lack of techniques to characterize soft-agar substrates. We employed a novel experimental approach utilizing colloidal probes and a specialized chamber which enabled us to measure diffusion near a no-slip boundary with more precise separation distance measurements than have been previously achieved. Additionally, we took measurements of colloidal diffusion near soft-agar surfaces for the first time. The colloidal diffusion measurements near agar surfaces

revealed that low percentage agars behave remarkably similarly to no-slip glass surfaces. Our findings suggest there is no relationship between viscous drag and agar concentration. We conclude that although there is a significant viscous drag near agar surfaces, it remains more or less constant between 0.45-4% agar wt/v. Therefore, changes in the viscous drag are unlikely to be responsible for the failure of *E. coli* to swarm on agar concentrations > 0.5%.

The methods and work discussed in Chapters 2 and 3 have led to new and further understanding of the swarming environment experienced by *E. coli* and how the cells change in response to this environment. Nevertheless, some questions remain unanswered. Porosity measurements for Eiken agar may help explain why the agar behaves in a manner similar to a no-slip surface. Separation distance measurements can be improved by visualizing agar with fluorescence microscopy. Additionally, the methods used in Chapter 3 can be expanded to probe diffusion, and indirectly, viscous drag, for a variety of surfaces. These measurements could be performed for biofilms, dental tissues, or other surfaces colonized by bacteria .

Finally, we have taken key steps toward the creation of a sticky filament in *C. crescentus*. Many of the mutants created in this study remain untested due to the vast size of the library that was created. Swimming assays should be carried out to screen the currently existing library. Additionally, optical tweezers should be employed to try and adhere cells to glass surfaces, as filaments have the potential to be sticky but not functional for swimming. Future studies should include a more rigorous modeling approach,

employing CHARMM or similar protein modeling software to identify mutations that would result in surface exposed residues but that do not negatively impact protein folding.

REFERENCES

1. Chawla, R., et al., *A Skeptic's Guide to Bacterial Mechanosensing.* J Mol Biol, 2020. **432**(2): p. 523-533.
2. Jefferson, K.K., *What drives bacteria to produce a biofilm?* FEMS Microbiol Lett, 2004. **236**(2): p. 163-73.
3. Stewart, P.S. and J. William Costerton, *Antibiotic resistance of bacteria in biofilms.* The Lancet, 2001. **358**(9276): p. 135-138.
4. Munoz-Dorado, J., et al., *Myxobacteria: Moving, Killing, Feeding, and Surviving Together.* Front Microbiol, 2016. **7**: p. 781.
5. Kim, W. and M.G. Surette, *Swarming populations of Salmonella represent a unique physiological state coupled to multiple mechanisms of antibiotic resistance.* Biological Procedures Online, 2003. **5**(1): p. 189-196.
6. Overhage, J., et al., *Swarming of Pseudomonas aeruginosa Is a Complex Adaptation Leading to Increased Production of Virulence Factors and Antibiotic Resistance.* 2008. **190**(8): p. 2671-2679.
7. Butler, M.T., Q. Wang, and R.M. Harshey, *Cell density and mobility protect swarming bacteria against antibiotics.* 2010. **107**(8): p. 3776-3781.
8. Kearns, D.B., *A field guide to bacterial swarming motility.* Nat Rev Microbiol, 2010. **8**(9): p. 634-44.
9. Partridge, J.D. and R.M. Harshey, *Swarming: Flexible Roaming Plans.* 2013. **195**(5): p. 909-918.
10. Eberl, L., S. Molin, and M. Givskov, *Surface Motility of Serratia liquefaciens MG1.* 1999. **181**(6): p. 1703-1712.
11. Berg, H.C., *Swarming Motility: It Better Be Wet.* Current Biology, 2005. **15**(15): p. R599-R600.
12. Alberti, L. and R.M. Harshey, *Differentiation of Serratia marcescens 274 into swimmer and swarmer cells.* Journal of bacteriology, 1990. **172**(8): p. 4322-4328.
13. Mattingly, A.E., et al., *Assessing Travel Conditions: Environmental and Host Influences on Bacterial Surface Motility.* 2018. **200**(11): p. e00014-18.
14. Wang, Q., et al., *Sensing wetness: a new role for the bacterial flagellum.* The EMBO Journal, 2005. **24**(11): p. 2034-2042.
15. Mariconda, S., Q. Wang, and R.M. Harshey, *A mechanical role for the chemotaxis system in swarming motility.* Molecular Microbiology, 2006. **60**(6): p. 1590-1602.
16. Burkart, M., A. Toguchi, and R.M. Harshey, *The chemotaxis system, but not chemotaxis, is essential for swarming motility in Escherichia coli.* 1998. **95**(5): p. 2568-2573.
17. Toguchi, A., et al., *Genetics of Swarming Motility in Salmonella enterica Serovar Typhimurium: Critical Role for Lipopolysaccharide.* 2000. **182**(22): p. 6308-6321.
18. Wu, Y., et al., *Periodic reversal of direction allows Myxobacteria to swarm.* 2009. **106**(4): p. 1222-1227.

19. Wu, Z., et al., *Swarming Motility Without Flagellar Motor Switching by Reversal of Swimming Direction in E. coli.* 2020. **11**(1042).
20. Copeland, M.F. and D.B. Weibel, *Bacterial swarming: a model system for studying dynamic self-assembly.* Soft Matter, 2009. **5**(6): p. 1174-1187.
21. McCarter, L., M. Hilmen, and M. Silverman, *Flagellar dynamometer controls swarmer cell differentiation of V. parahaemolyticus.* Cell, 1988. **54**(3): p. 345-51.
22. Lee, Y.-Y. and R. Belas, *Loss of FliL Alters Proteus mirabilis Surface Sensing and Temperature-Dependent Swarming.* 2015. **197**(1): p. 159-173.
23. Lauga, E., et al., *Swimming in Circles: Motion of Bacteria near Solid Boundaries.* Biophysical Journal, 2006. **90**(2): p. 400-412.
24. Zhang, H.P., et al., *Swarming dynamics in bacterial colonies.* EPL (Europhysics Letters), 2009. **87**(4): p. 48011.
25. Feitosa, M.I.M. and O.N. Mesquita, *Wall-drag effect on diffusion of colloidal particles near surfaces: A photon correlation study.* Physical Review A, 1991. **44**(10): p. 6677-6685.
26. Narayanan, J., J.-Y. Xiong, and X.-Y. Liu, *Determination of agarose gel pore size: Absorbance measurements vis a vis other techniques.* Journal of Physics: Conference Series, 2006. **28**: p. 83-86.
27. O'Toole, G.A. and G.C.L. Wong, *Sensational biofilms: surface sensing in bacteria.* Current Opinion in Microbiology, 2016. **30**: p. 139-146.
28. Prosser, B.L., et al., *Method of evaluating effects of antibiotics on bacterial biofilm.* Antimicrobial agents and chemotherapy, 1987. **31**(10): p. 1502-1506.
29. Nickel, J.C., et al., *Tobramycin resistance of Pseudomonas aeruginosa cells growing as a biofilm on urinary catheter material.* 1985. **27**(4): p. 619-624.
30. Nickel, J.C., et al., *Tobramycin resistance of Pseudomonas aeruginosa cells growing as a biofilm on urinary catheter material.* Antimicrob Agents Chemother, 1985. **27**(4): p. 619-24.
31. Trampuz, A. and A.F. Widmer, *Infections associated with orthopedic implants.* Curr Opin Infect Dis, 2006. **19**(4): p. 349-56.
32. Stanley, N.R. and B.A. Lazazzera, *Environmental signals and regulatory pathways that influence biofilm formation.* 2004. **52**(4): p. 917-924.
33. Li, G., et al., *Surface contact stimulates the just-in-time deployment of bacterial adhesins.* Molecular microbiology, 2012. **83**(1): p. 41-51.
34. Merker, R.I. and J. Smit, *Characterization of the Adhesive Holdfast of Marine and Freshwater Caulobacters.* Applied and Environmental Microbiology, 1988. **54**(8): p. 2078-2085.
35. Henrichsen, J., *Bacterial surface translocation: a survey and a classification.* Bacteriol Rev, 1972. **36**(4): p. 478-503.
36. Mobley, H.L. and R. Belas, *Swarming and pathogenicity of Proteus mirabilis in the urinary tract.* Trends Microbiol, 1995. **3**(7): p. 280-4.
37. Callegan, M.C., et al., *Role of swarming migration in the pathogenesis of bacillus endophthalmitis.* Invest Ophthalmol Vis Sci, 2006. **47**(10): p. 4461-7.

38. Yang, A., et al., *Influence of Physical Effects on the Swarming Motility of Pseudomonas aeruginosa.* Biophys J, 2017. **112**(7): p. 1462-1471.
39. Kim, W., et al., *Swarm-cell differentiation in Salmonella enterica serovar typhimurium results in elevated resistance to multiple antibiotics.* J Bacteriol, 2003. **185**(10): p. 3111-7.
40. Overhage, J., et al., *Swarming of Pseudomonas aeruginosa is a complex adaptation leading to increased production of virulence factors and antibiotic resistance.* J Bacteriol, 2008. **190**(8): p. 2671-9.
41. Hughes, A.C., and Kearns, D. B., *Swimming, swarming and sliding motility in bacillus subtilis.* , in *Cellular and Molecular Biology*. 2017, Poole: Caister Academic Press. p. 415–438.
42. Belas, R., *Biofilms, flagella, and mechanosensing of surfaces by bacteria.* Trends Microbiol, 2014. **22**(9): p. 517-27.
43. Harshey, R.M., *Bacterial motility on a surface: many ways to a common goal.* Annu Rev Microbiol, 2003. **57**: p. 249-73.
44. Darnton, N.C., et al., *Dynamics of bacterial swarming.* Biophys J, 2010. **98**(10): p. 2082-90.
45. Tuson, H.H., et al., *Flagellum density regulates Proteus mirabilis swarmer cell motility in viscous environments.* J Bacteriol, 2013. **195**(2): p. 368-77.
46. Harshey, R.M. and T. Matsuyama, *Dimorphic transition in Escherichia coli and Salmonella typhimurium: surface-induced differentiation into hyperflagellate swarmer cells.* Proc Natl Acad Sci U S A, 1994. **91**(18): p. 8631-5.
47. Wang, Q., et al., *Sensing wetness: a new role for the bacterial flagellum.* EMBO J, 2005. **24**(11): p. 2034-42.
48. Chen, B.G., L. Turner, and H.C. Berg, *The wetting agent required for swarming in Salmonella enterica serovar typhimurium is not a surfactant.* J Bacteriol, 2007. **189**(23): p. 8750-3.
49. Lele, P.P., B.G. Hosu, and H.C. Berg, *Dynamics of mechanosensing in the bacterial flagellar motor.* Proc Natl Acad Sci U S A, 2013. **110**(29): p. 11839-44.
50. Tipping, M.J., et al., *Load-dependent assembly of the bacterial flagellar motor.* mBio, 2013. **4**(4).
51. Terahara, N., et al., *Load- and polysaccharide-dependent activation of the Na(+)-type MotPS stator in the Bacillus subtilis flagellar motor.* Sci Rep, 2017. **7**: p. 46081.
52. Chawla, R., K.M. Ford, and P.P. Lele, *Torque, but not FliL, regulates mechanosensitive flagellar motor-function.* Sci Rep, 2017. **7**(1): p. 5565.
53. Schuster, S.C. and S. Khan, *The bacterial flagellar motor.* Annu Rev Biophys Biomol Struct, 1994. **23**: p. 509-39.
54. Zhao, R., et al., *FliN is a major structural protein of the C-ring in the Salmonella typhimurium flagellar basal body.* J Mol Biol, 1996. **261**(2): p. 195-208.
55. Macnab, R.M., *How bacteria assemble flagella.* Annu Rev Microbiol, 2003. **57**: p. 77-100.
56. Li, H. and V. Sourjik, *Assembly and stability of flagellar motor in Escherichia coli.* Mol Microbiol, 2011. **80**(4): p. 886-99.

57. Kojima, S. and D.F. Blair, *The bacterial flagellar motor: structure and function of a complex molecular machine.* Int Rev Cytol, 2004. **233**: p. 93-134.
58. Fukumura, T., et al., *Assembly and stoichiometry of the core structure of the bacterial flagellar type III export gate complex.* PLoS Biol, 2017. **15**(8): p. e2002281.
59. McMurry, J.L., J.W. Murphy, and B. Gonzalez-Pedrajo, *The FliN-FliH interaction mediates localization of flagellar export ATPase FliI to the C ring complex.* Biochemistry, 2006. **45**(39): p. 11790-8.
60. Paul, K., J.G. Harmon, and D.F. Blair, *Mutational analysis of the flagellar rotor protein FliN: identification of surfaces important for flagellar assembly and switching.* J Bacteriol, 2006. **188**(14): p. 5240-8.
61. Minamino, T., *Hierarchical protein export mechanism of the bacterial flagellar type III protein export apparatus.* FEMS Microbiol Lett, 2018. **365**(12).
62. Homma, M., et al., *FlgB, FlgC, FlgF and FlgG. A family of structurally related proteins in the flagellar basal body of Salmonella typhimurium.* J Mol Biol, 1990. **211**(2): p. 465-77.
63. Cohen, E.J., et al., *Nanoscale-length control of the flagellar driveshaft requires hitting the tethered outer membrane.* Science, 2017. **356**(6334): p. 197-200.
64. Gillen, K.L. and K.T. Hughes, *Negative regulatory loci coupling flagellin synthesis to flagellar assembly in Salmonella typhimurium.* J Bacteriol, 1991. **173**(7): p. 2301-10.
65. Calvo, R.A. and D.B. Kearns, *FlgM is secreted by the flagellar export apparatus in Bacillus subtilis.* J Bacteriol, 2015. **197**(1): p. 81-91.
66. Sarkar, M.K., K. Paul, and D. Blair, *Chemotaxis signaling protein CheY binds to the rotor protein FliN to control the direction of flagellar rotation in Escherichia coli.* Proc Natl Acad Sci U S A, 2010. **107**(20): p. 9370-5.
67. Pandini, A., F. Morcos, and S. Khan, *The Gearbox of the Bacterial Flagellar Motor Switch.* Structure, 2016. **24**(7): p. 1209-20.
68. Lele, P.P., et al., *Mechanism for adaptive remodeling of the bacterial flagellar switch.* Proc Natl Acad Sci U S A, 2012. **109**(49): p. 20018-22.
69. Paul, K., et al., *Architecture of the flagellar rotor.* EMBO J, 2011. **30**(14): p. 2962-71.
70. Branch, R.W., et al., *Adaptive remodelling by FliN in the bacterial rotary motor.* J Mol Biol, 2014. **426**(19): p. 3314-3324.
71. Delalez, N.J., R.M. Berry, and J.P. Armitage, *Stoichiometry and turnover of the bacterial flagellar switch protein FliN.* mBio, 2014. **5**(4): p. e01216-14.
72. Lele, P.P. and H.C. Berg, *Switching of bacterial flagellar motors [corrected] triggered by mutant FliG.* Biophys J, 2015. **108**(5): p. 1275-80.
73. Sourjik, V. and H.C. Berg, *Localization of components of the chemotaxis machinery of Escherichia coli using fluorescent protein fusions.* Mol Microbiol, 2000. **37**(4): p. 740-51.
74. Delalez, N.J., et al., *Signal-dependent turnover of the bacterial flagellar switch protein FliM.* Proc Natl Acad Sci U S A, 2010. **107**(25): p. 11347-51.

75. Konishi, M., et al., *Flagellar formation in C-ring-defective mutants by overproduction of FliI, the ATPase specific for flagellar type III secretion.* J Bacteriol, 2009. **191**(19): p. 6186-91.
76. Togashi, F., et al., *An extreme clockwise switch bias mutation in fliG of Salmonella typhimurium and its suppression by slow-motile mutations in motA and motB.* J Bacteriol, 1997. **179**(9): p. 2994-3003.
77. Datsenko, K.A. and B.L. Wanner, *One-step inactivation of chromosomal genes in Escherichia coli K-12 using PCR products.* Proc Natl Acad Sci U S A, 2000. **97**(12): p. 6640-5.
78. Ford, K.M., R. Chawla, and P.P. Lele, *Biophysical Characterization of Flagellar Motor Functions.* J Vis Exp, 2017(119).
79. Scharf, B.E., et al., *Control of direction of flagellar rotation in bacterial chemotaxis.* Proc Natl Acad Sci U S A, 1998. **95**(1): p. 201-6.
80. Yuan, J., et al., *Asymmetry in the clockwise and counterclockwise rotation of the bacterial flagellar motor.* Proc Natl Acad Sci U S A, 2010. **107**(29): p. 12846-9.
81. Blair, K.M., et al., *A molecular clutch disables flagella in the Bacillus subtilis biofilm.* Science, 2008. **320**(5883): p. 1636-8.
82. Lele, P.P., et al., *Response thresholds in bacterial chemotaxis.* Sci Adv, 2015. **1**(9): p. e1500299.
83. Fahrner, K.A., W.S. Ryu, and H.C. Berg, *Biomechanics: bacterial flagellar switching under load.* Nature, 2003. **423**(6943): p. 938.
84. Turner, L., et al., *Visualizing Flagella while Tracking Bacteria.* Biophys J, 2016. **111**(3): p. 630-639.
85. Liarzi, O., et al., *Acetylation represses the binding of CheY to its target proteins.* Mol Microbiol, 2010. **76**(4): p. 932-43.
86. Sourjik, V. and H.C. Berg, *Binding of the Escherichia coli response regulator CheY to its target measured in vivo by fluorescence resonance energy transfer.* Proc Natl Acad Sci U S A, 2002. **99**(20): p. 12669-74.
87. Ryu, W.S., R.M. Berry, and H.C. Berg, *Torque-generating units of the flagellar motor of Escherichia coli have a high duty ratio.* Nature, 2000. **403**(6768): p. 444-7.
88. Attmannspacher, U., B.E. Scharf, and R.M. Harshey, *FliL is essential for swarming: motor rotation in absence of FliL fractures the flagellar rod in swarmer cells of Salmonella enterica.* Mol Microbiol, 2008. **68**(2): p. 328-41.
89. Abrusci, P., et al., *Architecture of the major component of the type III secretion system export apparatus.* Nat Struct Mol Biol, 2013. **20**(1): p. 99-104.
90. Erhardt, M. and K.T. Hughes, *C-ring requirement in flagellar type III secretion is bypassed by FlhDC upregulation.* Mol Microbiol, 2010. **75**(2): p. 376-93.
91. Wang, Q., et al., *Gene expression patterns during swarming in Salmonella typhimurium: genes specific to surface growth and putative new motility and pathogenicity genes.* Mol Microbiol, 2004. **52**(1): p. 169-87.
92. Park, S.Y., et al., *Structure of FliM provides insight into assembly of the switch complex in the bacterial flagella motor.* Proc Natl Acad Sci U S A, 2006. **103**(32): p. 11886-91.

93. Paul, K., et al., *A molecular mechanism of direction switching in the flagellar motor of Escherichia coli.* Proc Natl Acad Sci U S A, 2011. **108**(41): p. 17171-6.
94. Tang, H. and D.F. Blair, *Regulated underexpression of the FliM protein of Escherichia coli and evidence for a location in the flagellar motor distinct from the MotA/MotB torque generators.* J Bacteriol, 1995. **177**(12): p. 3485-95.
95. Kuchma, S.L., et al., *Cyclic di-GMP-mediated repression of swarming motility by Pseudomonas aeruginosa PA14 requires the MotAB stator.* J Bacteriol, 2015. **197**(3): p. 420-30.
96. Lisicki, M. and G. Nägele, *Colloidal Hydrodynamics and Interfacial Effects*, in *Soft Matter at Aqueous Interfaces*, P.R. Lang and Y. Liu, Editors. 2016, Springer.
97. Goldstein, D., R. Handler, and L. Sirovich, *Modeling a No-Slip Flow Boundary with an External Force Field.* Journal of Computational Physics, 1993. **105**(2): p. 354-366.
98. Kang, C. and P. Mirbod, *Porosity effects in laminar fluid flow near permeable surfaces.* Physical Review E, 2019. **100**(1): p. 013109.
99. Trouilloud, R., et al., *Soft Swimming: Exploiting Deformable Interfaces for Low Reynolds Number Locomotion.* Physical Review Letters, 2008. **101**(4): p. 048102.
100. Rallabandi, B., et al., *Membrane-induced hydroelastic migration of a particle surfing its own wave.* Nature Physics, 2018. **14**(12): p. 1211-1215.
101. Lorentz, H.A., *Abhandlung über Theoretische Physik.* 1907.
102. Faxén, H., Ark. Mat. Astron. Fys., 1923. **17**(1).
103. Brenner, H., *The slow motion of a sphere through a viscous fluid towards a plane surface.* Chemical Engineerign Science, 1961. **16**: p. 242-251.
104. Goldman, A.J., R.G. Cox, and H. Brenner, *Slow viscous motion of a sphere parallel to a plane wall—I Motion through a quiescent fluid.* Chemical Engineerign Science, 1967. **22**: p. 637-651.
105. Goldman, A.J., R.G. Cox, and H. Brenner, *Slow viscous motion of a sphere parallel to a plane wall-II Couette flow.* Chemical Engineerign Science, 1967. **22**: p. 653-660.
106. Pralle, A., et al., *Local viscosity probed by photonic force microscopy.* Applied Physics A, 1998. **66**(1): p. S71-S73.
107. Faucheux, L.P. and A.J. Libchaber, *Confined Brownian motion.* Physical Review E, 1994. **49**(6): p. 5158-5163.
108. Lele, P.P., et al., *Colloidal diffusion and hydrodynamic screening near boundaries.* Soft Matter, 2011. **7**(15): p. 6844-6852.
109. Sadr, R., et al., *Diffusion-induced bias in near-wall velocimetry.* Journal of Fluid Mechanics, 2007. **577**: p. 443-456.
110. Huang, P. and K.S. Breuer, *Direct measurement of anisotropic near-wall hindered diffusion using total internal reflection velocimetry.* Physical Review E, 2007. **76**(4): p. 046307.
111. Kihm, K.D., et al., *Near-wall hindered Brownian diffusion of nanoparticles examined by three-dimensional ratiometric total internal reflection fluorescence microscopy (3-D R-TIRFM).* Experiments in Fluids, 2004. **37**(6): p. 811-824.

112. Huang, P., J.S. Guasto, and K.S. Breuer, *The effects of hindered mobility and depletion of particles in near-wall shear flows and the implications for nanovelocimetry.* Journal of Fluid Mechanics, 2009. **637**: p. 241-265.
113. Lobry, L. and N. Ostrowsky, *Diffusion of Brownian particles trapped between two walls: Theory and dynamic-light-scattering measurements.* Physical Review B, 1996. **53**(18): p. 12050-12056.
114. Ishii, K., T. Iwai, and H. Xia, *Hydrodynamic measurement of Brownian particles at a liquid-solid interface by low-coherence dynamic light scattering.* Optics Express, 2010. **18**(7): p. 7390-7396.
115. Plum, M.A., et al., *Probing dynamics at interfaces: resonance enhanced dynamic light scattering.* Optics Express, 2009. **17**(12): p. 10364-10371.
116. Holmqvist, P., J.K.G. Dhont, and P.R. Lang, *Colloidal dynamics near a wall studied by evanescent wave light scattering: Experimental and theoretical improvements and methodological limitations.* 2007. **126**(4): p. 044707.
117. Michailidou, V.N., et al., *Dynamics of Concentrated Hard-Sphere Colloids Near a Wall.* Physical Review Letters, 2009. **102**(6): p. 068302.
118. KATIYAR, A., et al., *A method for direct imaging of x–z cross-sections of fluorescent samples.* 2021. **281**(3): p. 224-230.
119. Grier, D.G., *Optical tweezers in colloid and interface science.* Current Opinion in Colloid & Interface Science, 1997. **2**(3): p. 264-270.
120. Crocker, J.C. and D.G. Grier, *Methods of Digital Video Microscopy for Colloidal Studies.* Journal of Colloid and Interface Science, 1996. **179**(1): p. 298-310.
121. Tarantino, N., et al., *TNF and IL-1 exhibit distinct ubiquitin requirements for inducing NEMO–IKK supramolecular structures.* Journal of Cell Biology, 2014. **204**(2): p. 231-245.
122. Choi, C.K., C.H. Margraves, and K.D. Kihm, *Examination of near-wall hindered Brownian diffusion of nanoparticles: Experimental comparison to theories by Brenner (1961) and Goldman et al. (1967).* 2007. **19**(10): p. 103305.
123. H., F., Arkiv. Mat. Astrom. Fys. , 1923.
124. Schneider, C.A., W.S. Rasband, and K.W. Eliceiri, *NIH Image to ImageJ: 25 years of image analysis.* Nature Methods, 2012. **9**(7): p. 671-675.
125. Silverman, M. and M. Simon, *Flagellar rotation and the mechanism of bacterial motility.* Nature, 1974. **249**: p. 73.
126. Blair, D.F. and H.C. Berg, *Restoration of torque in defective flagellar motors.* Science, 1988. **242**(4886): p. 1678-81.
127. Block, S.M., J.E. Segall, and H.C. Berg, *Adaptation kinetics in bacterial chemotaxis.* J Bacteriol, 1983. **154**(1): p. 312-23.
128. Block, S.M. and H.C. Berg, *Successive incorporation of force-generating units in the bacterial rotary motor.* Nature, 1984. **309**(5967): p. 470-472.
129. Iwazawa, J., Y. Imae, and S. Kobayasi, *Study of the torque of the bacterial flagellar motor using a rotating electric field.* Biophysical journal, 1993. **64**(3): p. 925-933.
130. Kuwajima, G., *Flagellin domain that affects H antigenicity of Escherichia coli K-12.* J Bacteriol, 1988. **170**(1): p. 485-8.

131. Yoshioka, K., S. Aizawa, and S. Yamaguchi, *Flagellar filament structure and cell motility of Salmonella typhimurium mutants lacking part of the outer domain of flagellin.* J Bacteriol, 1995. **177**(4): p. 1090-3.
132. Che, Y.S., et al., *Suppressor analysis of the MotB(D33E) mutation to probe bacterial flagellar motor dynamics coupled with proton translocation.* J Bacteriol, 2008. **190**(20): p. 6660-7.
133. Berg, H.C. and L. Turner, *Torque generated by the flagellar motor of Escherichia coli.* Biophysical Journal, 1993. **65**(5): p. 2201-2216.
134. Berry, R.M. and H.C. Berg, *Torque generated by the flagellar motor of Escherichia coli while driven backward.* Biophys J, 1999. **76**(1 Pt 1): p. 580-7.
135. Nakamura, S., et al., *Effect of intracellular pH on the torque-speed relationship of bacterial proton-driven flagellar motor.* J Mol Biol, 2009. **386**(2): p. 332-8.
136. Terahara, N., et al., *Load- and polysaccharide-dependent activation of the Na+-type MotPS stator in the Bacillus subtilis flagellar motor.* Scientific Reports, 2017. **7**: p. 46081.
137. Waterhouse, A., et al., *SWISS-MODEL: homology modelling of protein structures and complexes.* Nucleic Acids Research, 2018. **46**(W1): p. W296-W303.
138. Brooks, B.R., et al., *CHARMM: The Biomolecular Simulation Program.* Journal of computational chemistry, 2009. **30**(10): p. 1545-1614.
139. Thanbichler, M., A.A. Iniesta, and L. Shapiro, *A comprehensive set of plasmids for vanillate- and xylose-inducible gene expression in Caulobacter crescentus.* Nucleic Acids Research, 2007. **35**(20): p. e137-e137.
140. Faulds-Pain, A., et al., *Flagellin Redundancy in Caulobacter crescentus and Its Implications for Flagellar Filament Assembly.* Journal of Bacteriology, 2011. **193**(11): p. 2695-2707.
141. Lele, P.P., et al., *The flagellar motor of Caulobacter crescentus generates more torque when a cell swims backwards.* Nature Physics, 2015. **12**(2): p. 175-178.
142. Altschul, S.F., et al., *Basic local alignment search tool.* Journal of Molecular Biology, 1990. **215**(3): p. 403-410.
143. Cirino, P.C., K.M. Mayer, and D. Umeno, *Generating mutant libraries using error-prone PCR.* Methods Mol Biol, 2003. **231**: p. 3-9.
144. Humphrey, W., A. Dalke, and K. Schulten, *VMD: visual molecular dynamics.* Journal of molecular graphics, 1996. **14**(1): p. 33-38.
145. Emody, L., M. Kerenyi, and G. Nagy, *Virulence factors of uropathogenic Escherichia coli.* Int J Antimicrob Agents, 2003. **22 Suppl 2**: p. 29-33.
146. Lane, M.C., et al., *Role of motility in the colonization of uropathogenic Escherichia coli in the urinary tract.* Infect Immun, 2005. **73**(11): p. 7644-56.
147. Kao, C.Y., et al., *The complex interplay among bacterial motility and virulence factors in different Escherichia coli infections.* Eur J Clin Microbiol Infect Dis, 2014. **33**(12): p. 2157-62.
148. Berg, H.C., *The rotary motor of bacterial flagella.* Annu Rev Biochem, 2003. **72**: p. 19-54.

149. Gode-Potratz, C.J., et al., *Surface sensing in Vibrio parahaemolyticus triggers a programme of gene expression that promotes colonization and virulence.* Mol Microbiol, 2011. **79**(1): p. 240-63.
150. Silverman, M. and M. Simon, *Flagellar rotation and the mechanism of bacterial motility.* Nature, 1974. **249**(452): p. 73-4.
151. Segall, J.E., S.M. Block, and H.C. Berg, *Temporal comparisons in bacterial chemotaxis.* Proc Natl Acad Sci U S A, 1986. **83**(23): p. 8987-91.
152. Yuan, J. and H.C. Berg, *Resurrection of the flagellar rotary motor near zero load.* Proc Natl Acad Sci U S A, 2008. **105**(4): p. 1182-5.
153. Yuan, J., K.A. Fahrner, and H.C. Berg, *Switching of the bacterial flagellar motor near zero load.* J Mol Biol, 2009. **390**(3): p. 394-400.
154. Sowa, Y., et al., *Torque-speed relationship of the Na+-driven flagellar motor of Vibrio alginolyticus.* J Mol Biol, 2003. **327**(5): p. 1043-51.
155. Xing, J., et al., *Torque-speed relationship of the bacterial flagellar motor.* Proc Natl Acad Sci U S A, 2006. **103**(5): p. 1260-5.
156. Meacci, G. and Y. Tu, *Dynamics of the bacterial flagellar motor with multiple stators.* Proc Natl Acad Sci U S A, 2009. **106**(10): p. 3746-51.
157. Lele, P.P., et al., *The flagellar motor of Caulobacter crescentus generates more torque when a cell swims backward.* Nat Phys, 2016. **12**(2): p. 175-178.
158. Berg, H.C. and L. Turner, *Torque generated by the flagellar motor of Escherichia coli.* Biophys J, 1993. **65**(5): p. 2201-16.
159. Bai, F., et al., *Conformational spread as a mechanism for cooperativity in the bacterial flagellar switch.* Science, 2010. **327**(5966): p. 685-9.
160. Reid, S.W., et al., *The maximum number of torque-generating units in the flagellar motor of Escherichia coli is at least 11.* Proc Natl Acad Sci U S A, 2006. **103**(21): p. 8066-71.
161. Chen, X. and H.C. Berg, *Torque-speed relationship of the flagellar rotary motor of Escherichia coli.* Biophys J, 2000. **78**(2): p. 1036-41.
162. Turner, L., S.R. Caplan, and H.C. Berg, *Temperature-induced switching of the bacterial flagellar motor.* Biophys J, 1996. **71**(4): p. 2227-33.

APPENDIX A

SUPPLEMENTARY INFORMATION, CHAPTER 3

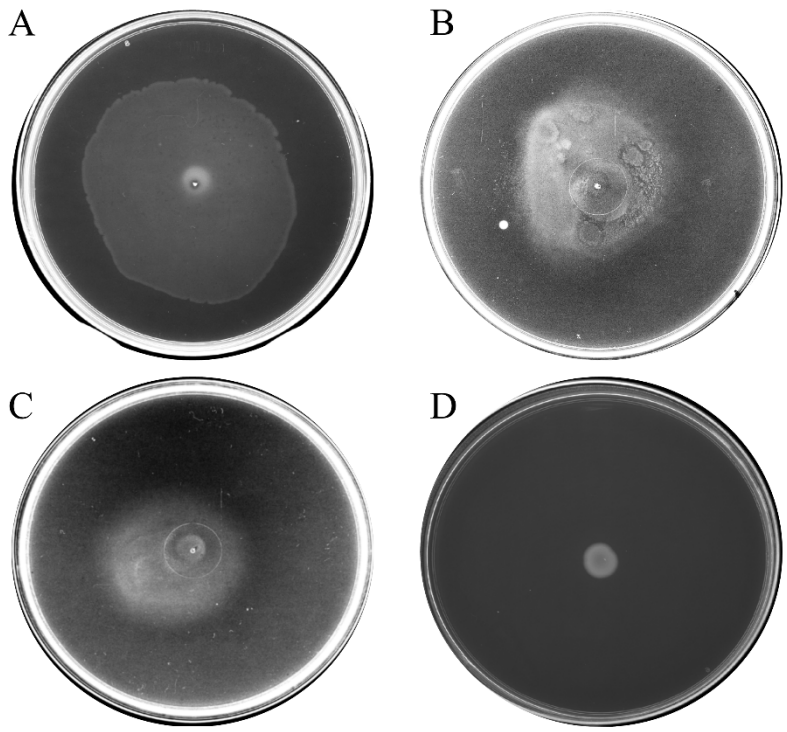

Figure A - 1 . Representative swarm assays for the strains of interest. (A) A standard swarm assay for the wildtype strain; (B) Swarming in CCW strain on agar surfaces that have additional moisture; (C) Swarming in CW strain on agar surfaces that have additional moisture; (D) Inability of the *fliG*^{CW} strain to swarm despite the addition of moisture to the agar surface.

Target	Primer set	Sequence (5' to 3')	Product
gapA	GapA_RT_Fwd	AAGTTGGTGTTGACGTTGTCGCTG	97
	GapA_RT_Rev	ATAACCACTTTCTTCGCACCAGCGG	
fliC	FliC_RT_Fwd	ACAGCCTCTCGCTGATCACTCAAA	100
	FliC_RT_Rev	GCGCTGTTAATACGCAAGCCAGAA	

Table A - 1. Primer information for qPCR studies.

Strain	ΔΔCt
Wildtype	2.01
CCW	0.77
$FliG^{CW}$	0.93

Table A - 2 qPCR results for agar-grown strains. ΔΔCt values > 2 were considered significant.

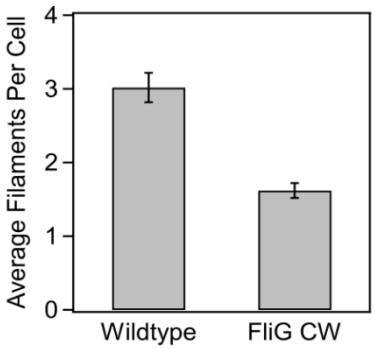

Figure A - 2. Filament counts via fluorescence-visualization in wildtype swarmer cells and FliG^{CW} cells grown on agar surfaces.

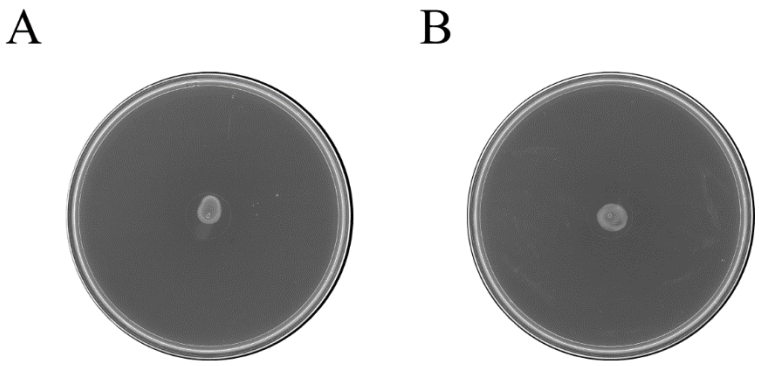

Figure A - 3. Representative swarms from overexpression assays. A) FliI overexpression in FliG^{CW} B) FlhA overexpression in FliG^{CW}

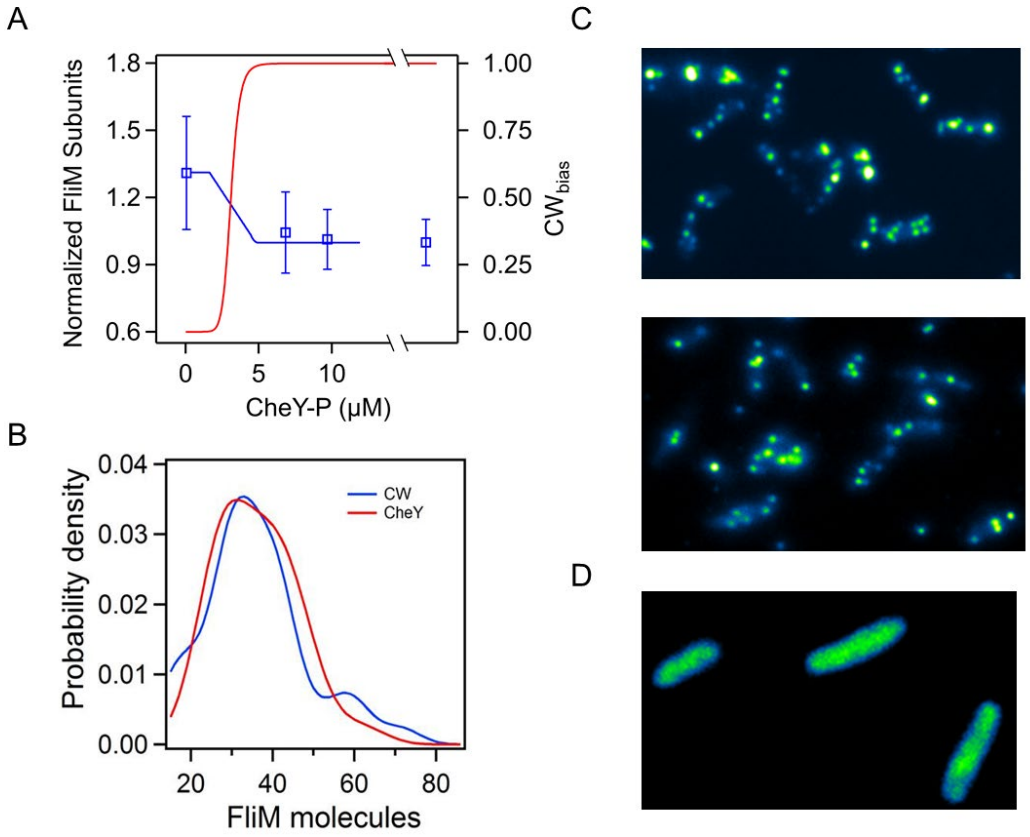

Figure A - 4. FliM molecule numbers for directional mutants. A) Dependence of normalized FliM numbers on the amount of intracellular CheY-P and CW_{bias} (Lele *et al*., 2012) There are fewer FliM molecules in CW-rotating motors and more FliM molecules in CCW-rotating motors. B) Comparisons between distributions of FliM molecules in rotating-flagellar motors in the $FliG^{CW}$ (blue) and a CW-only strain that carried the wildtype *fliG* allele and an excess pool of phosphorylated CheY (red). C) Representative images of putative flagellar preassemblies in cells belonging to a strain that carried the native *fliG* allele (left) and the $fliG^{CW}$ allele (right). The assemblies are indicated by localization of fluorescently-labeled FliM subunits. D) Representative image of a strain that lacks FliG and carries fluorescently-labeled FliM. As is clear, there is a complete lack of localization.

The $FliG^{CW}$ mutant employed in this work has been previously characterized in *E. coli* with the aid of biophysical assays (Lele *et al.,* 2012, Shrivastava *et al.* 2015, Lele and

Berg, 2015). Figure S3 indicates a subset of the data obtained via total internal reflection fluorescence microscopy (TIRF). Fig S3A indicates the dependence of the average number of FliM molecules in tethered motors as a function of cytoplasmic CheY-P levels (Figure 1, Lele *et al*., PNAS 2012). The last data point represents the mean numbers in a strain carrying the *fliG*^{CW} allele. In Figure S3B, the kernel density estimates are shown for the number of FliM molecules in two types of motors: FliG^{CW} motors (blue) and wildtype motors (FliG^{WT}) that are forced to rotate CW-only due to an excess pool of CheY-P molecules (Δ*cheRcheBcheZ*, *cheY-ptrc99A*). The difference in means was not statistically-significant at a 0.01 level. Figure S3C shows the similarities between localization of FliM molecules in the cell bodies in strains carrying the wildtype *fliG* (left) and the *fliG*^{CW} alleles on the genome. Together with the torque data in Figure 2, these results indicate that the assembly of FliM is not affected by the presence of the *fliG*^{CW} mutation, per se, although the direction of motor rotation certainly plays a role (Lele *et al*., PNAS 2012). Figure S4D indicates how cells that are unable to form a C-ring appear when FliM fusions are visualized via TIRF. Typically, the cells appear uniformly bright with no localization of the fluorescent signals.

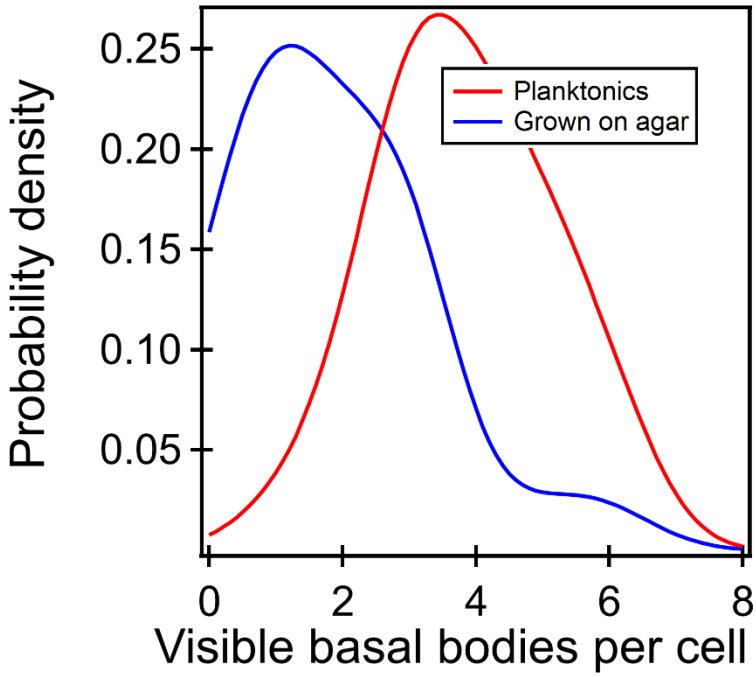

Figure A - 5. Flagellar preassemblies for directional mutants. Relative number of flagellar preassemblies in the planktonic and agar-grown cells in a strain that carried the native *fliG* and *fliM-eYFP-fliM* alleles and a constitutively-active form of CheY (CheYD13KY106W) on an inducible plasmid. The number of putative flagellar preassemblies were determined from TIRF measurements. There were fewer preassemblies in the agar-grown cells (1.84 ± 0.25 per cell, n = 31) relative to the planktonic cells (3.83 ± 0.21 per cell, n = 36). The difference in the means was significant ($p < 0.05$).

APPENDIX B

ERROR PRONE PCR PROTOCOL

The following protocol outlines the error-prone PCR that was carried out to make random mutations to sticky *fljK* constructs, as discussed in Chapter 4 of this document. This protocol was adapted based on published methods [143]. The expected error rate is 1-2 bp per 1 kb. Stocks and concentrations of reagents needed for this protocol are listed below.

1. Materials

1. Primers of interest (stored at -20°C, 100 µM)
2. Plasmid containing gene of interest to be amplified
3. 50X dNTP mixture: 10 mM each of dATP, dTTP, dCTP, and dGTP . Store 20 µL aliquots of this mixture to avoid excessive freeze/thaw cycles (store at −20°C)
4. dATP (10 mM, stored in 20 uL aliquots, 20°C)
5. dTTP (10 mM, stored in 20 uL aliquots, 20°C)
6. dCTP (10 mM, stored in 20 uL aliquots, 20°C)
7. dGTP (10 mM, stored in 20 uL aliquots, 20°C)
8. 10X Standard Taq Reaction Buffer (NEB)
9. 10X $MgCl_2$, 50 mM
10. $MnCl_2$, 1 mM
11. RNase free water
12. Betaine, 1M (used on a case by case basis)

2. Protocol

1. Prepare plasmid of interest, purify, measure concentration
2. For each PCR sample, add to the tube:
    a. 1 µL Taq polymerase
    b. 0.5 µL Forward primer
    c. 0.5 µL Reverse Primer
    d. 0.5 µL plasmid of interest
    e. 2 µL 50X DNTP mix
    f. Additional dNTPs (optional, I struggled to get reactions to work with addition of individual dNTPS. Unbalanced amounts of dNTPS promotes misincorporation. The outcomes of varying individual dNTP concentrations are well documented in the literature. See the methods paper I have referenced for additional information)
    g. 10 µL $MgCl_2$
    h. 1 µL $MnCl_2$ (Note: $MnCl_2$ concentration is the variable typically used to adjust error rate. It is a good idea to generate libraries with varying $MnCl_2$ concentrations in your PCR. Add last to prevent precipitation)
    i. 20 µL Standard Taq Buffer
    j. RNase free water, balance to 100 µL
    k. Optional – add betaine if secondary structures are of concern

3. Run Error-Prone PCR program as outlined in referenced method's paper (Note: I found I needed to increase the extension step to ~double the recommended step, this will need to be changed on a case-by-case basis)
4. Isolate DNA for cloning and transform into the plasmid of interest as necessary, based on lab protocols.

Note: You will likely need to run the PCR at a temperature gradient to determine the best running temperature. I found that Tm predictions for regular PCR did not work for error-prone PCR.

Primers of interest:

fljK_P1_Nde1: GGAATTCCATATGGAATTCCTCTTTCGTTATGGCG

fljK_P4_XbaI: GCTCTAGAGTCCCTGCCCCTTAACG

APPENDIX C

PROTEIN BY PROTEIN ALIGNMENT OF FLJK AND FLIC

Range 1: 6 to 171

Score	**Expect**	**Method**	**Identities**	**Positives**	**Gaps**
47.8 bits(112)	**1e-10**	**Compositional matrix adjust.**	**49/172(28%)**	**95/172(55%)**	**12/172(6%)**

```
Query  5    INTNSLSLLTQNNLNKSQSALGTAIERLSSGLRINSAKDDAAGQAIANRFTANIKGLTQA  64
            INTN+ +++  NLN + S L T  +R+++G +I SAKD+ A  A A  +A    T A
Sbjct  6    INTNAGAMIALQNLNGTNSELTTVQQRINTGKKIASAKDNGAIWATAKNQSA-----TAA  60

Query  65   SRNA-NDGISIAQTT----EGALNEINNNLQRVRELAVQSANSTNSQSDLDSIQAEITQR  119
             S NA  D +  Q+T     A + I + L +++E A+ +++++ + +  ++++++
Sbjct  61   SMNAVKDSLQRGQSTIDVALAAGDTITDLLGKMKEKALAASDTSLNTASFNALKSDFDSL  120

Query  120  LNEIDRVSGQTQFNGVKVLAQDNTLTIQVGAN-DGETIDIDLKQINSQTLGL  170
             ++I++ +  +FNGV + A  +T  +  AN DG   ++ K I+  +GL
Sbjct  121  RDQIEKAATNAKFNGVSI-ADGSTTKLTFLANSDGSGFTVNAKTISLAGIGL  171
```

Range 2: 190 to 274

Score	**Expect**	**Method**	**Identities**	**Positives**	**Gaps**
35.8 bits(81)	**1e-06**	**Compositional matrix adjust.**	**26/85(31%)**	**41/85(48%)**	**0/85(0%)**

```
Query  412
IDAALAQVDTLRSDLGAVQNRFNSAITNLGNTVNNLTSARSRIEDSDYATEVSNMSRAQI  471
             ID AL      + LG      ++ +T +G   ++L +    + D+D A E + +   Q
Sbjct  190
IDTALQTATNKLASLGTSSVGLDTHLTFVGKLQDSLDAGVGNLVDADLAKESAKLQSLQT  249
Query  472  LQQAGTSVLAQANQVPQNVLSLLR*  496
               QQ G   L+ ANQ   ++LSL R*
Sbjct  250   KQQLGVQALSIANQSSSSILSLFR*  274
```

Range 3: 2 to 34

Score	**Expect**	**Method**	**Identities**	**Positives**	**Gaps**
21.6 bits(44)	**0.035**	**Compositional matrix adjust.**	**17/41(41%)**	**25/41(60%)**	**8/41(19%)**

```
Query  81   ALNEINNNLQRVRELAVQSANSTNSQSDLDSIQAEITQRLN  121
            ALN IN N   +  +A+Q+ N TNS+  L ++Q    QR+N
Sbjct  2    ALNSINTNAGAM--IALQNLNGTNSE--LTTVQ----    QRIN  34
```

APPENDIX D

FLJK SWISS MODEL REPORT

The SWISS model report below provides an evaluation of the model. The model scores shown below are QMEAN: scores of -4 or below indicate low quality of the model. The "Local Quality" plot shows, for each residue of the model (reported on the x-axis), the expected similarity to the native structure (y-axis).

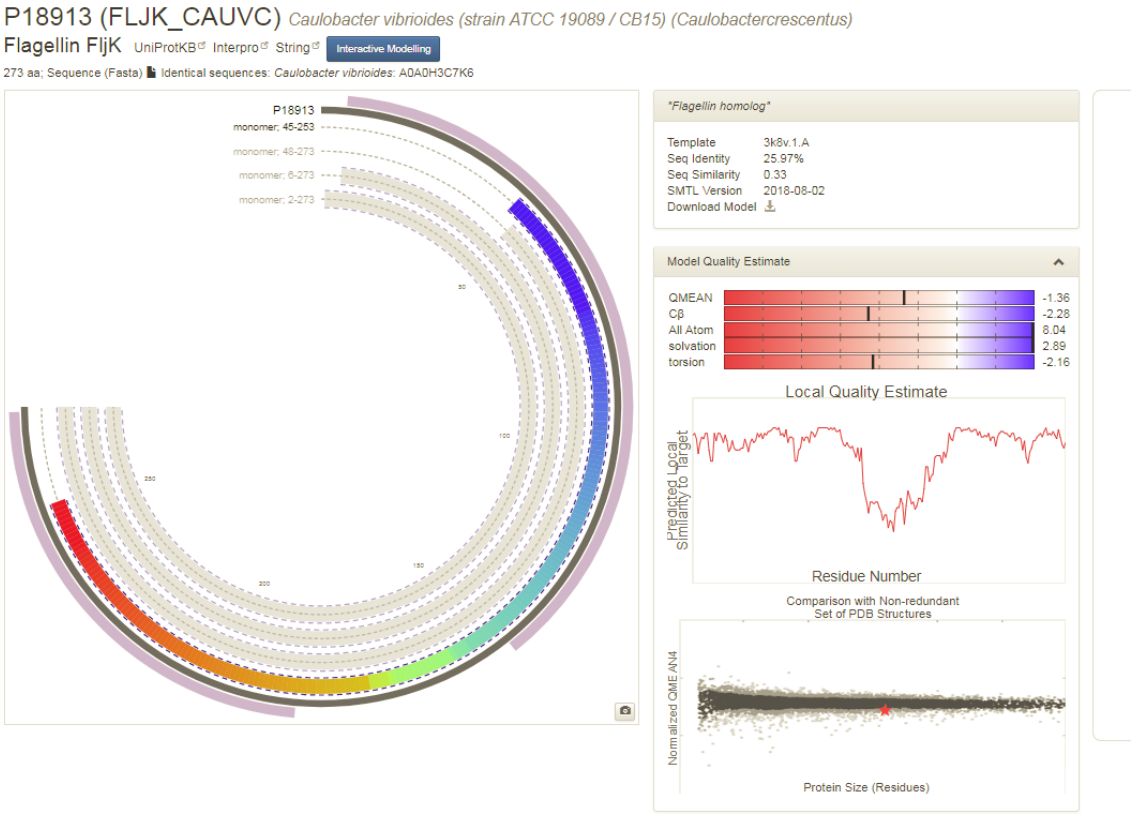

APPENDIX E

BIOPHYSICAL CHARACTERIZATION OF FLAGELLAR MOTOR FUNCTIONS[1]

INTRODUCTION

Flagellar motors enable cells to swim by rotating helical extracellular filaments. The amount of torque the motor can generate for a given length of the flagellum (*i.e.*, the viscous load) determines the swimming speeds. On the other hand, its ability to switch the direction of rotation controls cell migration in response to chemicals, a process known as chemotaxis. Chemotaxis and motility being virulence factors [145-147], flagellar motors have been well-characterized over the years [148]. Mounting evidence now suggests that the motor acts as a mechanosensor — it mechanically detects the presence of solid substrates [21, 49]. This ability likely helps in triggering surface colonization and infections [21, 149]. As a result, the mechanisms whereby the motor senses surfaces and initiates signaling are of significance [8, 42].

The flagellar motor can be readily studied by tethering the flagellum to a substrate and observing cell rotation. Such tethering was first achieved by Silverman and Simon, who worked with a polyhook mutant in *E. coli* and successfully attached hooks to glass substrates with anti-hook antibodies [150]. The tethered-cell assay enabled researchers to study the responses of the motor-switch to a variety of chemical stimuli. For example, Segall and co-workers chemically stimulated tethered cells with the aid of iontophoretic pipettes. The corresponding changes in CW_{bias} (the fraction of the time motors spin

[1] *Reprinted with permission from "Biophysical Characterization of Flagellar Motor Functions" by K. Ford, R. Chawla, P.P. Lele. Vis Exp, 2017(119)

clockwise, CW) enabled them to measure the kinetics of adaptation in the chemotaxis network [127, 151]. While the tethered cell assay was effective in studying switch responses, it was only able to offer insights into motor mechanics over a limited range of viscous loads [126]. To overcome this problem, Ryu and co-workers tethered spherical, latex beads to filament stubs on cells stuck to surfaces. The beads were then tracked using back-focal interferometry with weak optical traps [87]. By working with beads of different sizes, researchers could study the motor over a much wider range of loads. This assay was later improved by Yuan and Berg, who developed a photomultiplier-based bead-tracking technique combined with laser dark-field illumination. Their method enabled tracking of tethered gold nanobeads that were so tiny (~ 60 nm) that the external viscous resistances were lower compared to the internal viscous resistances to rotation [152, 153]. This led to the measurements of the maximum achievable speeds in *E. coli* (~ 300 Hz). In *V. alginolyticus*, similar bead assays enabled measurements of the spinning rates at intermediate viscous loads (~ 700 Hz) [154]. By enabling measurements of motor responses over the entire possible range of viscous loads (from zero-load to near-stall), the bead-assays provided an important biophysical tool to understand the torque-generation process [155, 156].

Recently, we modified the Yuan-Berg assay to include optical tweezers that enabled us to apply precise mechanical stimuli to individual motors [49]. Using this technique, we showed that the force-generators that rotate the motor are dynamic mechanosensors — they remodel in response to changes in viscous loads. It is possible that such load-sensing triggers cell differentiation into swarming bacteria, although the mechanisms remain

unclear. It is also likely that the flagellar motors in other species are also mechanosensitive [157], although direct evidence is lacking. Here, we discuss the photomultiplier-based (PMT) approach for tracking the rotation of latex beads tethered to flagellar filaments [152]. In comparison to tracking with ultrafast cameras, the photomultiplier-setup is advantageous because it is relatively straightforward to track single beads in real-time and over long durations. It is particularly useful when studying long-time remodeling in flagellar motor complexes due to environmental stimuli [82]. Though we detail protocols specifically for *E. coli*, they can be readily adapted for studying flagellar motors in other species.

PROTOCOL

1. Cell Preparation

1. Grow overnight cultures of the desired strain carrying the sticky *fliC* allele[152, 158] in Tryptone Broth (TB, 1% Peptone, 0.5% NaCl) followed by inoculation at 1:100 dilution in 10 mL fresh TB. Grow the culture at 33 °C in a shaker incubator until OD_{600} = 0.5.
2. Pellet the cells at 1,500 x g for 5 - 7 min and re-disperse the pellet vigorously in 10 mL of filter sterilized motility buffer (MB; 10 mM phosphate buffer: 0.05-0.06 M NaCl, 10^{-4} M EDTA, 1 μM methionine, pH 7.0).
3. Repeat step 1.2 two more times and re-disperse the final pellet in 1 mL MB.
4. Shear the suspension by passing back and forth ~ 75 times between two syringes with 21 to 23-gauge adapters connected by polyethylene tubing (7 - 12 cm long, 0.58 mm inner diameter). Limit the total time for shearing to 30 - 45 s.

5. Centrifuge the sheared cells at 1,500 x g for 5-7 min and re-disperse the pellet in 100 - 500 µL of MB.

2. Slide Preparation

1. Prepare an imaging chamber by sandwiching two double-sided adhesive tapes between a cover-slip and a microscope slide. For chemotaxis assays, employ any microfluidic chamber that enables the exchange of MB and chemical stimulants.
2. Add 0.01% poly-L-lysine solution in the chamber and after 5 min gently rinse the surfaces with MB (80 - 100 µL).
3. Add 40 µL of the cell suspension into the chamber and allow sufficient time for attachment to the glass surface (7 - 8 min). Flow out unstuck cells by adding 100 µL MB on one side of the chamber, while wicking the solution with a filter paper from the other side.
4. Add 10 - 15 µL of latex beads into the chamber and allow the beads adequate time to settle and attach to the cells (7 - 8 min). Gently rinse with 100 µL of MB, as described in step 2.3, to remove unstuck beads. Use a range of bead-sizes for the experiments so long as a good contrast is available.

3. Bead Tracking

1. Place the sample on a microscope stage and scan the surface for beads attached to motors. Use a 40X phase objective to make observations although phase microscopy is not necessary. Alternatively, employ bright-field imaging so long as sufficient contrast is maintained to clearly distinguish a bright bead on a dark background.

2. Once a bead has been selected, move the stage laterally to position the bead in a pre-determined corner as shown in **Figure E-1B**. Position beads at the same corner to ensure that the direction of rotation of the bead is correctly known. The ideal bead trajectory is approximately circular but elliptical trajectories are admissible.
3. Maintain the sampling frequency higher than twice the rotational frequency of the motor to avoid errors associated with aliasing. In this work, use a motor that was rotating at 50 Hz and sample at frequencies that were 10 times higher (500 Hz), to obtain a smooth signal.

4. Data Analysis

1. Center and scale the PMT output voltages and correct ellipticity in the trajectories with affine transformations if needed [159]. Use a power-spectrum analysis to determine rotation rates [154].
2. Determine polar angles, $\theta(t) = \text{atan}\,(y(t)/x(t))$. Determine the variations in motor speeds and switching over time by calculating $\omega = \frac{1}{2\pi} d\theta/dt$ [14].
3. Employ a median filter to smooth the motor speed data. A filter window over two full rotations is recommended [159, 160].

The photomultiplier setup is shown in **Figure E-1A**. It is important that the PMTs have high sensitivities over the range of wavelengths scattered by the beads of interest. The PMTs employed here operate in the visible and near-infrared ranges, and were able to detect light scattered by beads illuminated by a halogen light source. The optimum lighting conditions and supply voltages will vary from one setup to another. For the setup used in

this work, a PMT gain ~ 10^4 - 10^5 proved adequate. Each photomultiplier was covered except for a 3 x 1 mm slit positioned in front of the photomultiplier. The slits limit the region in the cell-sample from which light can enter the photomultipliers, and the two slits are orthogonal to one another. When a rotating bead is positioned at the correct location (**Figure E-1B**), the amount of light entering the photomultiplier increases as the bead comes in the view and decreases as its circular path takes it away from the view. The frequencies of the sinusoidal PMT voltage outputs indicate the speed of rotation and the phase differences between the two signals indicate the direction of rotation. The use of an oscilloscope to display the PMT outputs enables visualization of bead trajectories in real-time.

The time-varying PMT signals, y(t) and x(t), from a representative motor are shown in **Figure E-2A**. The orthogonality of the two slits introduces a phase lag between the two signals. The signal amplitudes depend on the signal-to-noise ratio as well as the eccentricity of rotation. The corresponding trajectories of the bead are indicated in **Figure E-2B**.

A histogram of the speeds measured from a representative motor in a *cheY*- deleted strain is shown in **Figure E-3A**. The deletion ensures that flagellar motors cannot switch and rotate exclusively counterclockwise (CCW). The average speed from this particular motor was 60 Hz and the measured speeds are consistent with previous reports for motors tethered with 1 μm beads [161]. The bead was first positioned at the lower right corner, as seen in the schematic in **Figure E-1B**. The corresponding angular speed is shown in **Figure E-3B** (top panel). Positioning the bead to the adjacent lower left corner resulted

in inversion of the sign on the motor speeds (bottom panel). Thus, moving the bead to an adjacent corner will change the observed direction of motor rotation. In this regard, diagonally opposite corners are identical. It is therefore crucial to know the location of the bead during measurements to correctly determine the switching dynamics. **Figure E-3C** shows repeated transitions of a wild-type motor between the two directions of rotation. Custom codes for data-acquisition software were adapted from prior work to record the data on a computer[152]. The PMT output was AC-coupled and low-pass filtered with a cutoff frequency of 100 Hz. Real-time tracking was enabled by connecting the filtered outputs to an oscilloscope.

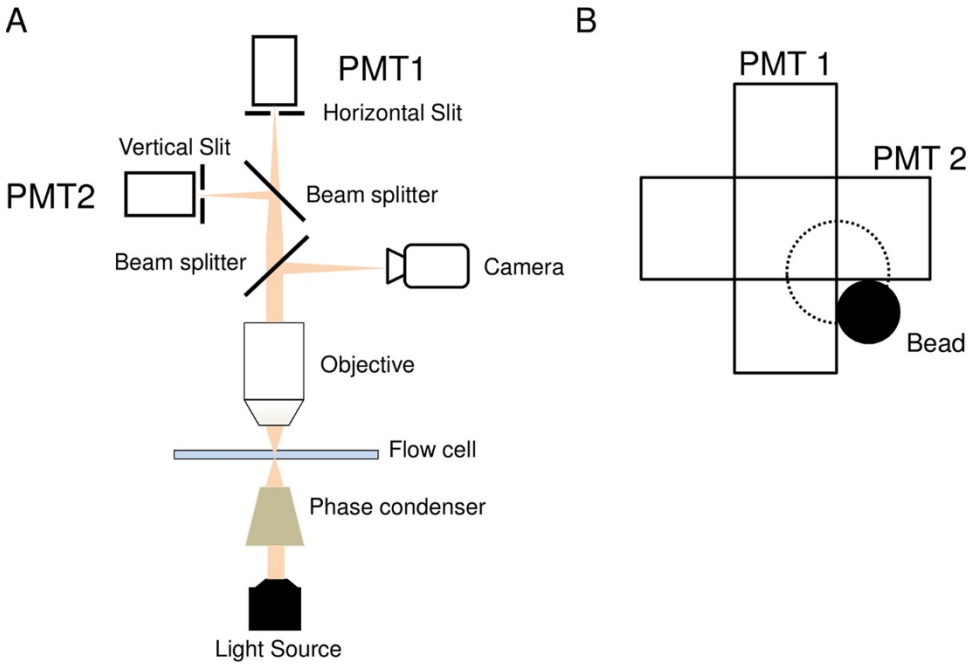

Figure E - 1: Bead-tracker Setup. A) Schematic of the PMT-based tracking setup. B) The ideal position of the bead (black sphere) relative to the two orthogonal slits. The trajectory is indicated by the dotted lines. The eccentricity *e* is the radius of the dotted circle.

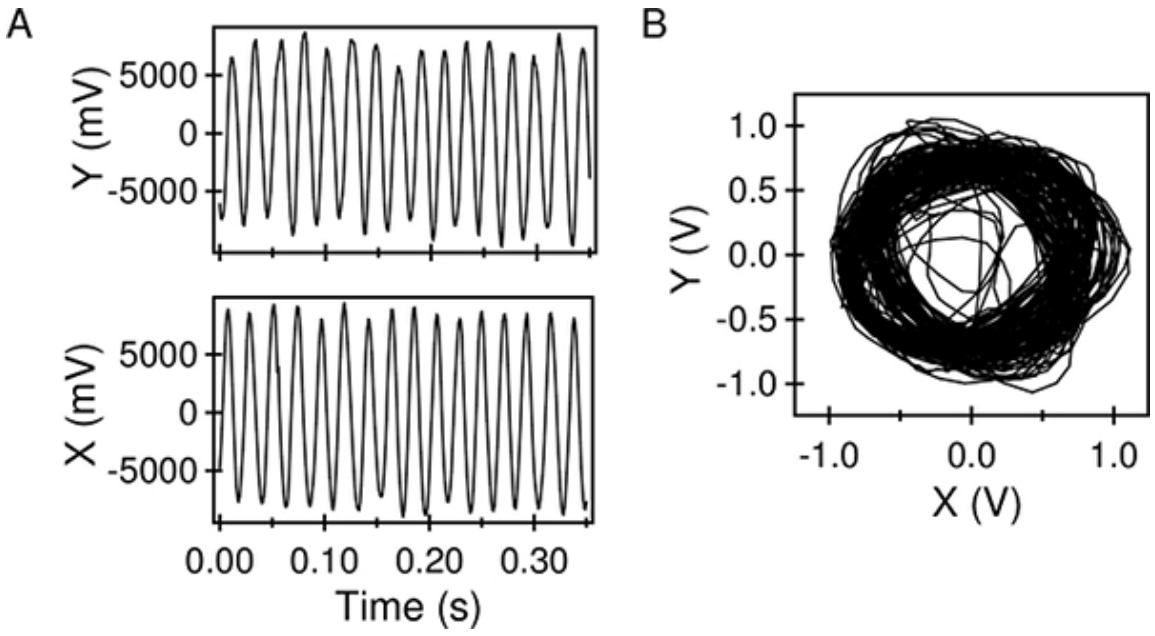

Figure E - 2: PMT Outputs. A) Low-pass filtered outputs from the two photomultipliers, after centering/scaling. B) The bead trajectories obtained from the PMT data, sampled over 3 s.

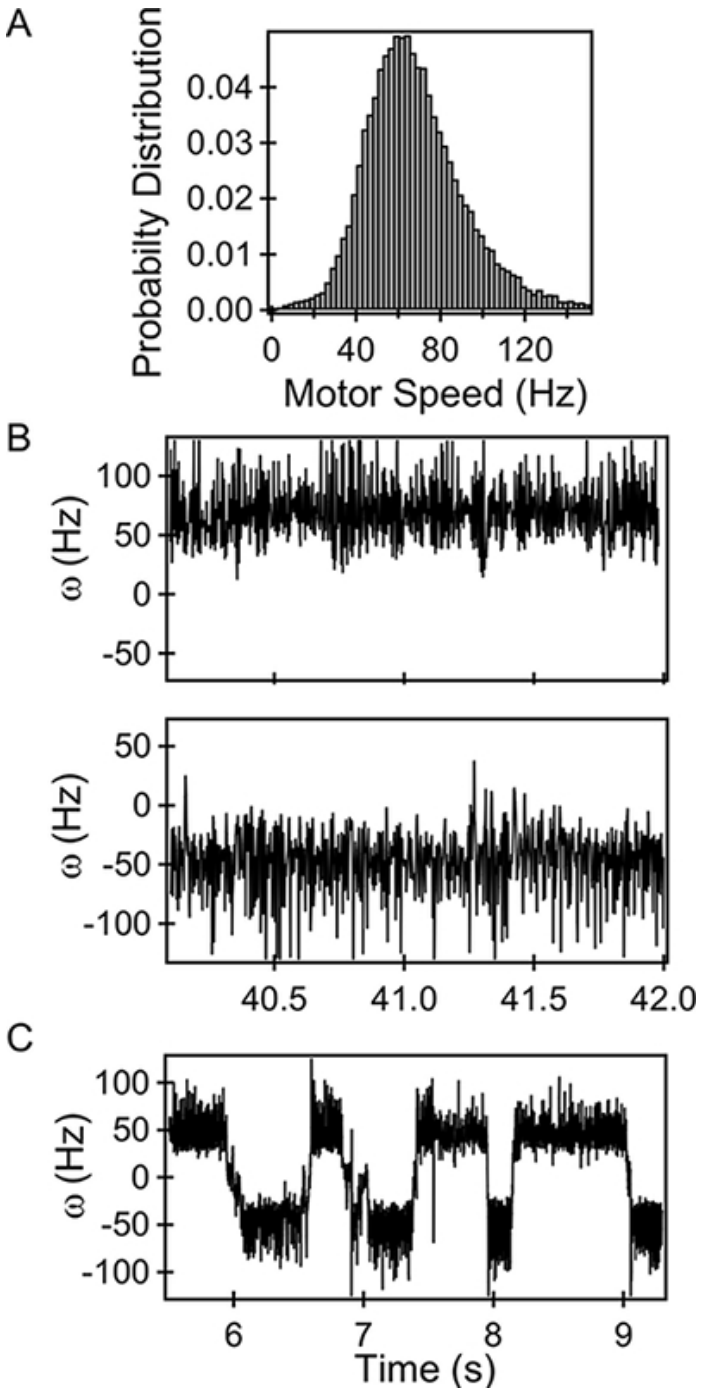

Figure E - 3: Bead Trajectories. A) Histogram of CCW-only speeds of a representative motor. B) Rotational speeds of a CCW-only motor imaged at lower right corner (top panel). Rotational speeds of the same motor when positioned at the lower left corner (bottom panel). C) Switching in a representative wild-type motor.

DISCUSSION

In order to facilitate tethered bead-tracking and correct estimation of motor-torques, the following information should be reviewed. When performing these measurements with flagellated cells, shearing is a critical step. Shearing reduces the flagellar filament to a mere stub, thereby ensuring that the viscous load on the motor is predominantly due to the bead and can be estimated within 10% error [16]. Shearing also improves the chances of finding circular trajectories with tightly distributed eccentricities (< bead diameter [87]). Improper shearing results in wayward trajectories, which compounds errors in tracking and in the calculation of viscous drags, as well as resulting in poor signal-noise ratios. The use of an oscilloscope allows rapid elimination of such data. Since the biomechanical properties of flagellar filaments are expected to vary with species, shearing methods will likely need to be adapted to ensure adequate shearing in the bacteria of interest. An effective way of reducing errors associated with shearing is to work with cells that lack the genes that encode the filament proteins. Probe beads can then be attached directly to the hook via anti-hook antibodies.

Finding a bead that is appropriately tethered can be challenging. This is because most beads in the field of view will either be stuck to the cell bodies or the glass surface. Such beads can be readily brought into sharp focus. Other beads will appear to vibrate or rotate visibly with large amplitudes or large eccentricities (> 1.5 - 2x bead diameter). These are typically tethered to flagellar filaments that have not been fully sheared or rotate in a plane that is inclined to the focal plane. Sampling of such beads will typically result in higher noise, and time-variations in viscous loads may result in an underestimation of motors

torques for a given bead-size. A small fraction of tethered beads will undergo random motion; these are merely undergoing Brownian rotation. A fraction of the beads will appear blurred and cannot be brought in focus easily. These are most likely to be motors which have been tethered appropriately and are the motors of interest.

Among the limitations of single-motor tracking such as the one described here is the inability to conduct high-throughput experiments. A high-speed camera that images a larger region of interest can be advantageous in this regard. Other limitations include errors associated with multiple signals arising out of closely spaced rotating beads in the field of view of the PMTs. Finally, errors in determination of the correct position of the recorded bead with respect to the two photomultiplier slits will result in imprecise estimation of the switching dynamics.

Advantages of the setup described here include the ability to track the rotation of the beads over long durations and in real-time. This enables rapid elimination of error-prone trajectories, something that maybe difficult to achieve with ultrafast cameras. Additionally, with a few modifications this setup can be integrated with assays designed to subject cells to a variety of stimuli. Combined with thermoelectric cooling [162], the technique can be employed to measure the responses of individual motors to thermal stimuli. Integration with optical tweezers can enable the measurements of remodeling of individual motors in response to mechanical stimuli, as has been done recently [49]. Finally, the adaptation of the motor to chemical stimulants can be measured with the use of an appropriate perfusion chamber and pumps [127].

A majority of known bacterial species are motile and flagellar-mediated motility is predominant in nature. The methods demonstrated here are expected to continue to aid in the development of insights into structural-remodeling and the adaptability of the flagellar motor.